INSTITUTE FOR APPLIED ANALYSIS AND NUMERICAL SIMULATION

CHAIR OF APPLIED ANALYSIS

SIMULATION TECHNOLOGY DEGREE COURSE

Bachelor thesis

Numerical Simulations on Momentum Coupling and Orbit Modification in Laser-Based Debris Removal

First Supervisor

Jun.-Prof. Dr. Andrea Barth

Institute for Applied Analysis and Numerical Simulation

Second Supervisor

Apl. Prof. Dr. Johannes Roth

Institute for Functional Materials and Quantum Technologies

Third Supervisor

Dr. Stefan Scharring

German Aerospace Center - Institute of Technical Physics

Submitted by

Author	Lukas EISERT
Matriculation number	2864082
SimTech-Nr.	82
Submission date	March 2018

Selbstständigkeitserklärung

Hiermit versichere ich, dass ich die vorliegende Bachelorarbeit selbständig verfasst habe. Ich versichere, dass ich keine anderen als die angegebenen Quellen benutzt und alle wörtlich oder sinngemäß aus anderen Werken übernommenen Aussagen als solche gekennzeichnet habe, und dass die eingereichte Arbeit weder vollständig noch in wesentlichen Teilen Gegenstand eines anderen Prüfungsverfahren gewesen ist.

Datum, Unterschrift

One proposed method of space debris removal is the irradiation of particles with laser pulses. If the laser energy is high enough, ablation of the surface is occurring and a recoil is formed. With the generated change in momentum and thus change in velocity a debris particle could be de-orbited. At the moment, only rough analytical estimations of this method are available neglecting the exact shape of the particle and the spatial fluence distribution within the laser beam. Based on an existing ablation model, the laser-matter interaction program 'EXPEDIT' was therefore improved and used as a module for a space debris de-orbit simulation. Together, this provides an experimental validated toolbox for further investigations in debris de-orbit strategies.

Abbreviations

CAD	Computer-aided Design
CMS	Center of Mass System
CPU	Central Processing Unit
DLR	German Aerospace Center
ECEF	Earth-Centered Earth-Fixed
ECI	Earth Centered Inertial
ESA	European Space Agency
EXPEDIT	Examination Program for irregularly shaped Debris Targets
lmi	laser-matter-interaction
LASER	Light Amplification by Stimulated Emission of Radiation
GPU	Graphics Processing Unit

Greek Symbols

α	angular distraction of the laser beam direction
β	confidence level
γ	sidereal angle
ϵ	eccentricity
ϵ_0	confidence interval error estimation
ζ	zenith angle
λ	laser wavelength
Λ	longitude
μ	gravitational parameter
ρ	material density
σ	angular beam distortion error, statistical standard deviation, parameter for the Gaussian beam
σ_P	angular pointing error
σ_S	angular seeing error
σ_T	angular tracking error
τ	pulse length
ϕ	latitude
Φ	laser fluence in the beam profile
Φ'	laser fluence at the target
Φ_{max}	maximum laser fluence within the beam profile
$\vec{\omega}$	debris rotational velocity
Ω	rotation operator

Latin Symbols

a, b, c	laser-matter-interaction fitting parameter
a_μ	-
A	illuminated target surface
A_x	experimental cross-sectional area
c_m	laser-mater-interaction coupling coefficient
C_n^2	atmospheric turbulence strength
d_L	laser beam diameter
d_D	debris diameter
e	elevation
$\tilde{e}$	modified elevation
E_L	laser pulse energy
E_{orb}	specific orbital energy
E_{rot}	rotational energy
f	laser repetition rate
h	simulation step size
h_{orb}	step size of the velocity verlet algorithm
h_{rot}	step size of the rotation propagator step size
h_L	grid size of the ray tracing algorithm
i	step index within a transit
I	laser intensity
$\mathbf{I}$	inertia tensor in ECI
$\mathbf{J}$	inertia tensor in CMS
$\mathbf{J}'$	normalized inertia tensor in CMS
Δk	beam displacement at the target
$\vec{k}$	laser direction
$\hat{k}$	normalized laser direction
$\vec{k}_\sigma$	distorted beam direction
l	index of run within a Monte Carlo simulation
$\vec{L}$	debris angular momentum
L_c	characteristic length
m_D	mass of the debris particle
m_A	mass of the ablated material
M	overall number of runs within a Monte Carlo simulation
$\hat{n}$	surface normal vector
N	overall number of surface elements, rays and laser pulses within a transit
$\vec{p}$, $\vec{p}_D$	momentum of the debris particle
$\vec{p}_A$	momentum of the ablated material
r	radius of the beam
r_0	fried parameter
r_e	earth radius
$\vec{r}$	position within the laser beam, position of a volume element inside a particle
$\mathbf{R}$	debris orientation matrix
t	time
$\vec{t}_1, \vec{t}_2$	orthogonal tangential vectors
$\vec{v}$, $\vec{v}_D$	velocity of the debris particle

$\vec{v}_A$	velocity of the ablated material
V	volume
W_0	beam diameter at sending telescope
x, y, z	debris main axis length
x_0	ablation limit
x_a	apogee
x_p	perigee
$\vec{x}$, $\vec{x}_D$	position of the debris particle
$\vec{x}_L$	position of the laser station

Contents

[1] The Introduction is part of the Propaedeuticum

1 Introduction[2]

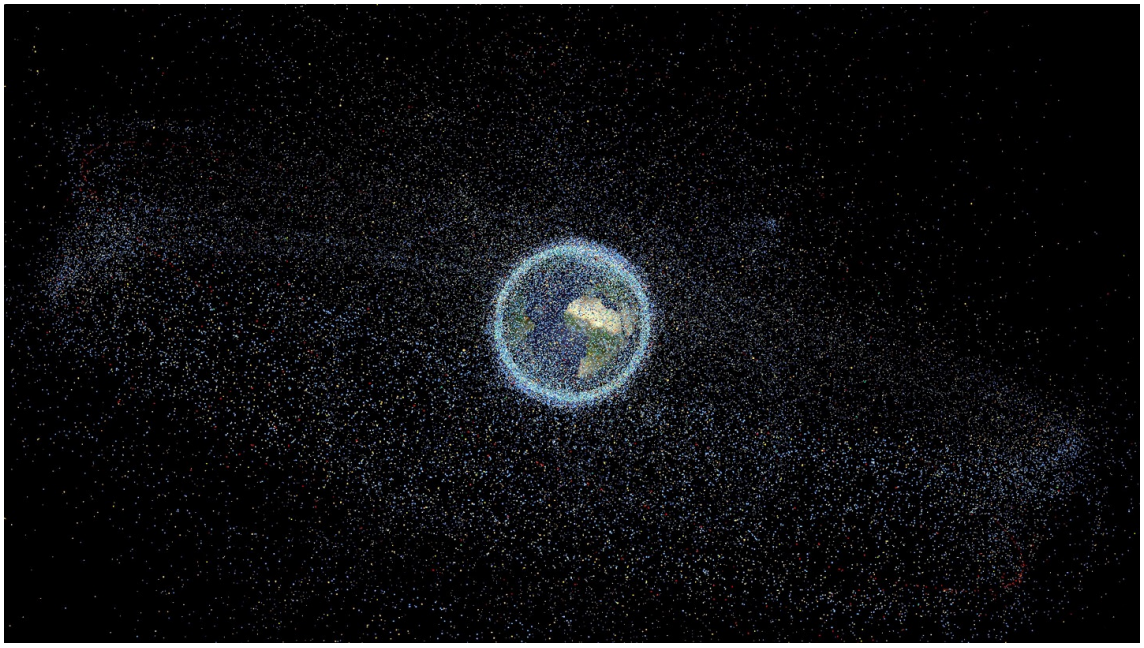

Figure 1: Particle distribution of space debris around the earth according to simulations. Visualization was taken from [1] Indicated are all objects larger than $1cm$. Large debris populations are visible in the low earth orbit (LEO) with altitudes up to $2000km$ and the geostationary orbit(GEO) at around $35700km$

Space debris becomes a more and more serious threat for satellites and manned space missions as well. Even though modern spacecrafts are armoured, a collision with a relative small particle ($\approx 1cm$) can be fatal to the craft due to high impact velocities (up to several $\frac{km}{s}$). Space debris includes every human made uncontrolled object in space, which mainly comes from old rocket stages, dead satellites but collisions with space debris too. [1] The first two origins can be avoided by alternated space mission designs which avoid the emission of further debris and the disposal of dead satellites by active de-orbiting or parking on graveyard orbits. But there is still a need for removal of debris which is already in the orbit. Especially because the remaining debris leads to a further increase of dangerous particles by collisions with satellites and other debris. But how can existing debris be removed? Near the earth surface there is still enough atmosphere, braking and so de-orbiting each object. This mechanism is slower the farther the particles are away from the surface. In the low earth orbit (LEO) with altitudes up to $2000km$ above the surface, a particle already needs more than 100 years until it burns up in the atmosphere leading so to a kind of debris 'layer' around the globe which can be seen in figure 1. This thesis will be focused on the removal of this layer using a ground-based-laser stations to ablate material from the debris surface, inducing so a change in orbit which hopefully results in an earlier re-entry.

At the moment, only rough models are available to predict the alternation of the debris orbit which assume a constant laser fluence distribution and neglecting the exact shape of the object. [2] Previous numerical simulations showed [3], that the shape of the particle has an important influence on the direction and the absolute value of the momentum generation. Be-

[2]The Introduction is part of the Propaedeuticum

cause the momentum generation is highly dependent on the orientation of the particle, the recoupling with the angular speed is non-trivial leading so to a quite chaotic behaviour. Therefore, it is in the focus of this thesis to develop a model of the debris removal process, taking into account an arbitrary debris shape, debris spin and the fluence distribution of the laser beam. Because of the stochastic nature we will use a Monte Carlo approach to quantise the alternation of the orbit with mean and standard deviations. To calculate the interaction between the laser beam and the particle, the model from [3] was used. To reduce computation costs, the model was reimplemented in a parallelized way and GPU based. This model provides future studies with a validated tool to investigate the change in orbit due to pulsed laser irradiation. Initial simulations also showed, that in general the process leads to a significant orbit lowering. First, we want to take a closer look on the different aspects of space debris (Section 1.1). Then an introduction to the ablation process is given (Section 1.2) including methods to actually calculate the change in momentum (Section 1.3). Afterwards, the model of the simulation is stated (Section 2) followed by the numerical improvements on the laser-matter-interaction(lmi) module called 'Expedit' (Section 3) and the numerical implementation of the removal model (Section 4). The implemented code is then validated (Section 5) and used for a few example simulations (Section 6).

1.1 Space Debris

In this section, we want to focus on the space debris itself. For the model we should know how to describe the dynamics of the particles including the orbit and the rotational speed. For the interaction with the laser, the material and the shape are of interest.

Orbit

For the analytical description of the orbit we use Keplerian orbits. This is a simple model which only takes the gravitational force into account, leading so to simple elliptical orbits which are a quite good description of real orbits. Because this is a problem of classical mechanics, the whole trajectory is fully described by an initial position $\vec{x}$ and an initial velocity $\vec{v} = \frac{\partial \vec{x}}{\partial t}$ of the object at a specific point in time t_0. But this is not a good choice to describe the orbit because position and velocity are altering along the same orbit and the form of the orbit is not intuitively clear. As we deal with 6 degrees of freedom (which are position and velocity), one should be able to find a set of 6 constant and independent parameter to fully describe an orbit. Starting with the position and velocity, one can get the following quantities which stay constant along the orbit. Note that this derivation has been taken from [4, Ch. 4.4]. First, the specific energy E_{orb} is given by

$$E_{orb} = \frac{\vec{v}^2}{2} - \frac{\mu}{|\vec{x}|} \tag{1.1}$$

where μ is the standard gravitational parameter of the earth. This is the kinetic energy minus the gravitation potential divided by the particle mass. With the orbital angular momentum h

$$\vec{h} = \vec{x} \times \vec{v} \tag{1.2}$$

which is supposed to be a conserved quantity, the eccentricity ϵ of the elliptical orbit can be calculated using

$$\epsilon = \sqrt{1 + 2E_{orb}\frac{\vec{h}^2}{\mu^2}} \quad . \tag{1.3}$$

For $\epsilon = 0$ the ellipse becomes an circle. The major axis of the ellipse a is then

$$a = -\frac{\mu}{2E_{orb}} \quad . \tag{1.4}$$

One can then finally calculate two points of interest: perigee x_p and apogee x_a

$$x_p = (1-\epsilon)\cdot a \tag{1.5}$$

$$x_a = (1+\epsilon)\cdot a \tag{1.6}$$

These two quantities, describe the largest and smallest distance to the earth centre. So one has to reduce the perigee to de-orbit the object which is possible by reducing the velocity of the object by a certain value Δv. From [5], we can estimate the needed Δv to approx $150\frac{m}{s}$. (This is of course only valid for our LEO de-orbiting scenario) With ϵ and a one has now the full description of the orbital ellipse. But one still needs four more quantities which derivation is not nearer explained in this thesis. Those are, two angles which define the orientation of the orbital plane

- inclination

- longitude of the ascending node

and two quantities to define the orientation of the ellipse in the orbital plane and the position of the object along the ellipse

- argument of periapsis
- true anomaly

To combine this parameter in a standardized way, the Two-Line Elements Format (TLE) was introduced by NASA, containing this 6 orbit parameter together with a time reference (epoch) and factors containing information about friction. In the following there is example for a TLE describing the orbit of the International Space Station

```
1 25544U 98067A    17316.88912037   .00004714   00000−0   78401−4 0   9996
2 25544   51.6432   17.0202 0004414 112.0154 227.8246 15.54134137 84874
```

Freely accessible TLEs of objects are published by celestrak [6]. There, one can find orbits of debris produced by the collision between Iridium 33 and Kosmos 2251 in 2009 which could be used in simulations later on.

Material

The next open issue is the material. On the one hand, it influences the mass and so the momentum of the particle. On the other hand, it will have an influence on the interaction with the laser too. The simplest approach to clear this question is to investigate the used materials in astronautics. Because the debris comes from the gadgets which were send to space, it can be assumed that the debris basically consist of the same material. An investigation was carried out in [7]. The materials were grouped according to their densities: high density (steel, cooper) medium density (paint, aluminium) and low density (plastics, fibreglass). By taking the size into account, medium densities are dominating for particles diameters $> 1cm$. Because satellites are anyway protected against smaller objects, it seems to be sufficient to constrain the debris material to aluminium.

Shape

An even bigger question is the shape of the particles. Up to now, nobody has caught a sufficient sample of real space debris to make clear statements on how space debris is actual formed. But to investigate the behaviour of particles under laser irradiation it is essential to have at least a rough idea about the shape of the object. To get information about the shape, crash tests can be performed, which means that the collisions are reproduced in a laboratory and recorded afterwards. We will focus on the results of such an experiment done in 2007 in cooperation between the Kyushu University and NASA [8]. Three cubic micro satellites with an edge length of $20cm$ were fired with $3cm$ aluminium projectiles with an impact speed of $1.7km/s$. However, it was not possible to get models of the remnants so one must focus on the more abstract results released with the paper. For this, three main axes are defined. The largest diameter is called x. The largest diameter along x is called y and the diameter orthogonal to x and y is called z. Each point of the scatter plot in Figure 2 represents a remnant of the experiment. Plotted are the ratio $\frac{x}{y}$ and $\frac{y}{z}$. With this we got a rough estimate of the shape of the resulting object. There are two types: plates ($\frac{x}{y} \approx 1$ and $\frac{y}{z} > 2$) and rods ($\frac{x}{y} \approx 10$ and $\frac{y}{z} \approx 10$). Because the ratios do not define the actual size of the object, we have to find a scale to get the actual values for x, y and z. To do so, the characteristic length L_c is defined by

$$L_c = \frac{x+y+z}{3} \tag{1.7}$$

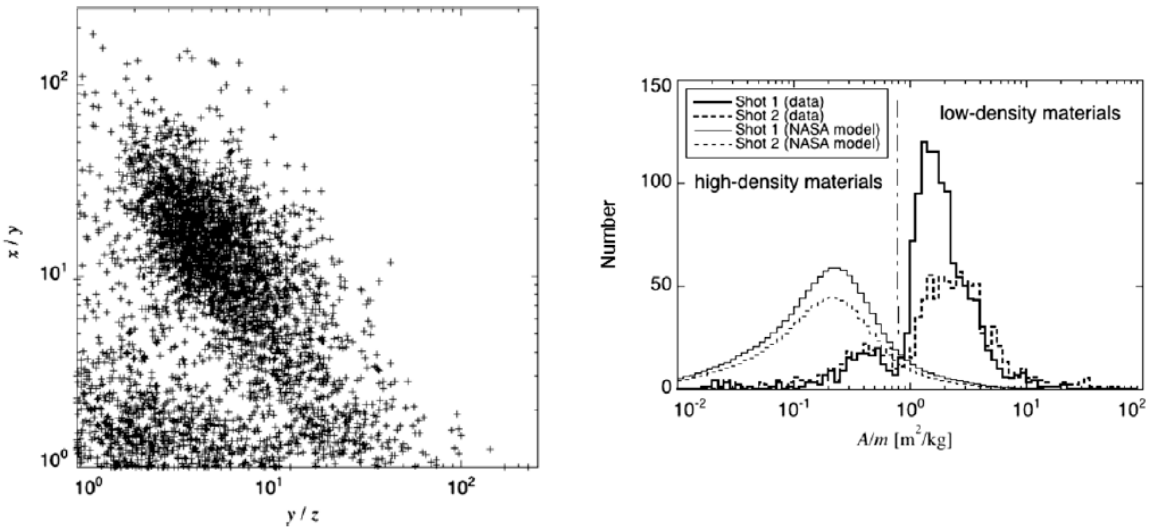

Figure 2: Crash test results taken from [8]. Left: Distribution of the ratios. One can see the plates represented by the crosses at the bottom of the plot and the rods by the cloud in the middle. Right: Histogram of the particle abundance with a certain area to mass ratio.

which is the average out of the three main axes. With this length scale, the average cross-sectional area A_x can be defined

$$A_x = \begin{cases} 0.540242 \cdot L_c^2, & L_c < 0.00167 \\ 0.5556945 \cdot L_c^2.0047077, & L_c \geq 0.00167 \end{cases} \tag{1.8}$$

giving an effective average value for the visible surface area. From the experimental results plotted in Figure 2, the axes x, y, z can be extracted. Estimations for the cross-sectional area A_x can be gained by using the measured values for the area mass A/m and multiplying it by the measured mass of the remnants. To reproduce objects with these properties, ellipsoids have been used as the simplest and most symmetric solid body with three degrees of freedom.

Rotational Speed

Finally we want to have a look on the rotation of the particles. Most of the particles arise from collisions [9]. Because these collisions are clearly not always perfectly central, the particles should eventually have a non-neglectable initial rotational speed. But how could someone measure this rotation? A possibility is to observe the light curve. This means, that the time variation of the reflected light is measured. This could be either the light of the sun or of a laser beam. Because the reflection depends on the orientation the resulting light curve can be directly used to estimate the rotation speed. But this method has two drawbacks: First one could get a proper sine-like curve only for ideal objects like a plate. For example, a ball would lead to no alternation in light at all, independent on the rotational speed. An irregular object would lead to a quite fuzzy curve. The second problem is, that the amount of reflected light depends of course on the surface size of the object. The majority of the particles are quite small and so detection of a light curve is equally more difficult.

1.2 Momentum Generation by Laser Ablation

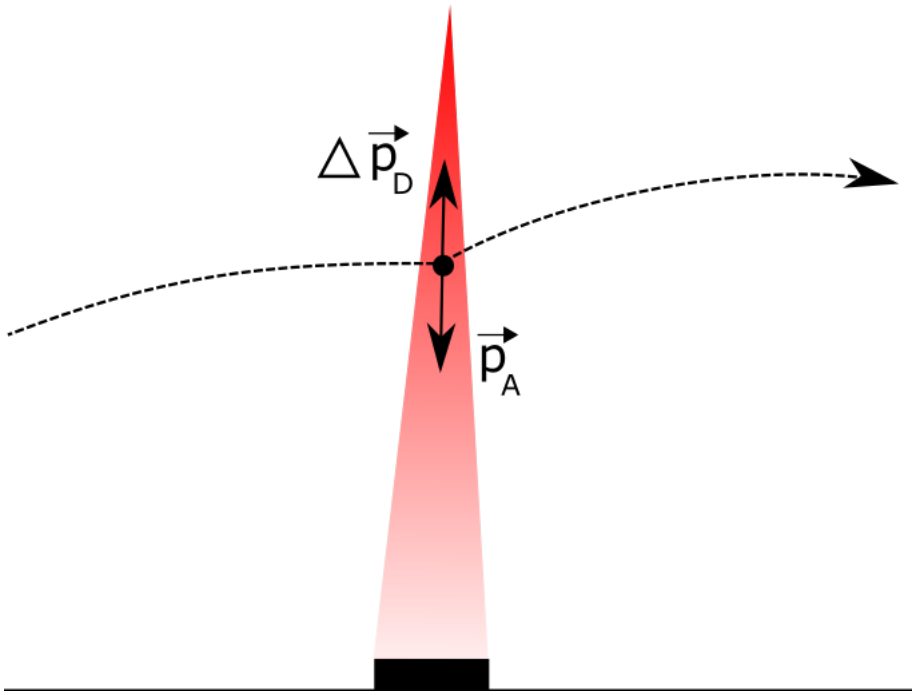

Figure 3: A focused laser pulse inducing a change in momentum $\Delta\vec{p}_D$ and so a change in orbit.

The method which is discussed in this thesis, is space debris removal using a focused pulsed laser beam. The general idea of this is to use a laser beam to ablate material of the debris surface. This material is pushed away with a certain velocity $\vec{v}_A$. Because conservation of momentum is valid, the change in momentum of the debris is then the same as of the ablated material with switched sign

$$\Delta\vec{p}_D = -\vec{p}_A = -m_A\vec{v}_A \quad . \tag{1.9}$$

The change in velocity of the object $\Delta\vec{v}_D$ can then be calculated

$$\Delta\vec{v}_D = \frac{\Delta\vec{p}_D}{m_D} \tag{1.10}$$

with the debris mass m_D. To fully understand this process, a short introduction to the laser technology is given. Afterwards the ablation process is closer explained leading then to existing methods of momentum generation calculations.

LASER

Laser is an acronym of light amplification by stimulated emission of radiation which makes it possible to create a monochromatic, coherent and highly focused beam. In contrast to thermal light sources like light bulbs, the light is not emitted spontaneously in different wavelengths and phases. Instead, one uses the quantum effect called stimulated emission. This states, that a photon can stimulate an excited quantum system to emit a photon with the same phase and wavelength. To use this effect, a medium consisting of excitable multi-level quantum systems is needed, for example vibrations of CO_2 molecules. One has to bring energy into the medium

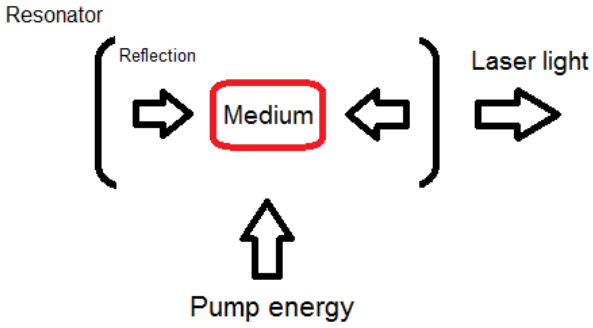

Figure 4: Systematic structure of a laser

to excite this systems from the ground state to a higher state of energy (called pumping). For instance a gas discharge lamp, cathode rays or another laser can be used. After this the quantum systems are in a higher energy state than they should be according to thermal equilibrium (which is called population inversion), but we still have no laser because the exited systems would simply emit spontaneously. So, the second important component of a laser system is the so-called resonator, which are two mirrors at each end of the medium in the simplest case, preventing the spontaneously emitted photons from leaving the device. Instead, they stay inside the medium stimulating the emission of more photons. There are now two possible modes of operation:

First there is the continuous wave mode in which the power leaving the resonator as laser beam is equal to the power which is brought into the system by pumping minus thermal power loss. This means the power of the resulting laser beam is constant and limited by the pumping power and the quantum efficiency of the laser medium. For higher energy one might be interested in using the medium as a kind of energy reservoir. This is done by switching the resonator off and pump until a full population inversion is reached. When the resonator is then again activated, the complete energy that was saved in the medium is almost released at once. This is called the pulse mode. For our purposes we need high energies at the target, so a pulsed laser system is the natural choice. The resulting laser beam can be parametrized by the following properties:

- wavelength λ
- pulse length τ
- pulse energy E_L

Assuming that properties are constant, although dealing with instabilities of them is also a topic in laser physics, there is still no information on how the energy is distributed over time $t \in [0, \tau]$ and the profile of the beam $\vec{x}$. Therefore, the intensity $I(\vec{x}, t)$ is needed, giving the power density at each point and time. For the ablation process, only the profile at the target is needed. Because the pulse time proposed for debris removal is short (in the ns range), the temporal behaviour of the laser pulse is neglected and the ablation process is assumed to be instantaneous. To apply this to the laser, the intensity is integrated over time leading to the fluence for each pulse

$$\Phi(\vec{x}) = \int I(\vec{x}, t)\, dt \tag{1.11}$$

which is the energy density at each point of the laser profile. With integration over the profile, one can get the energy of the pulse

$$E_L = \int \Phi(\vec{x})\, dA \quad . \tag{1.12}$$

But how can one define a meaningful $\Phi(\vec{x})$? Of course, one could measure a real profile (cf. Section 3.2), but because a laser system suitable for debris removal does not exist yet, it is not practical for this thesis. Instead, the theoretical solutions of the electromagnetic wave equations is used, which leads in the simplest case to a Gaussian profile. This can be seen as a kind of optimum because real profiles are superpositions of several transversal laser modes leading to a much more flattened profile. The Gauss profile can be described analytically by

$$\Phi(r) = \frac{E_L}{a} e^{-\frac{r^2}{2\sigma^2}} \quad . \tag{1.13}$$

For this profile, σ is used as parameter and describes the broadness of the beam. a is the normalization constant and can be calculated with an integration of the Gaussian over the two-dimensional profile

$$a = \int_0^{2\pi} \int_0^{\infty} e^{-\frac{r^2}{2\sigma^2}} r\, dr\, d\Phi = 2\pi\sigma^2 \tag{1.14}$$

leading to the final expression

$$\Phi(r) = \frac{E_L}{2\pi\sigma^2} e^{-\frac{r^2}{2\sigma^2}} \quad . \tag{1.15}$$

It is easy to see, that with this definition, the fluence is non zero for arbitrary r. How can one define a diameter of this profile? To do this, the commonly used 'Power in the bucket' definition is used. This means that the radius r of the laser spot is defined as the distance, where the fluence has fallen on the $1/e^2$ of the maximum Φ_{max}

$$\Phi_{max} = \Phi(0) = e^2 \Phi(r) \quad . \tag{1.16}$$

Using Equation (1.15), this leads to a relationship between σ and the beam spot diameter d_L

$$\sigma = \frac{r}{2} = \frac{d_L}{4} \tag{1.17}$$

making it possible to replace σ in Equation (1.15) with the diameter

$$\Phi(r) = \frac{8E_L}{\pi d_L^2} e^{-\frac{8r^2}{d_L^2}} \quad . \tag{1.18}$$

Furthermore, the maximum Φ_{max} is given by

$$\Phi_{max} = \frac{8E_L}{\pi d_L^2} \quad . \tag{1.19}$$

To mention it again, this still is a simple approximation of the real beam profile. Especially after a long propagation through atmosphere the real profile may heavily differ from a Gaussian one.

Laser ablation

In this section we will have a closer look on the ablation process itself. The laser induces energy to the surface of the object. During pulse durations in the ns regime, the energy has not enough time to further penetrate the object. Instead, it leads to a heating of the surface and so to a vaporization of the top layer. The resulting hot plasma (a mixture of ions and electrons) is pushed away from the target surface by the vaporization pressure leading so to a recoil. The whole process could be described and simulated in an atomistic way and thus on the scale of the single atoms in the material lattice. But this would lead to unreasonable computation costs for our purposes, because the interaction has to be calculated for each pulse. Instead, we are looking for an effective theory, which approximates the results of a more complex theory. According to [10] one can simplify the process by defining a coupling coefficient which connects the incident energy to the resulting change in momentum

$$c_m = \frac{\Delta p}{E_L} \quad . \tag{1.20}$$

If the coupling coefficient c_m and the energy E_L are known, Δp can be calculated. Using that the ablation recoil is directed perpendicular away from the object surface [11], the change in momentum $\Delta\vec{p}$ can be expressed as

$$\Delta\vec{p}_D = -\vec{p}_A = -c_m E_L \hat{n} \tag{1.21}$$

with the surface normal $\hat{n}$. But this formula is only valid if the coupling coefficient c_m is constant and the surface flat with a constant surface normal $\hat{n}$. The later could be addressed by writing the equation in a local form for each point on the curved surface. But what are the dependencies on the coupling coefficient? From the one-dimensional Polly-2T model [12], which pays attention to the temporal development of the electron gas and the ion lattice temperature in the material during the laser pulse, following dependencies have been found:

- surface material
- angle of incidence
- polarization of the ray
- pulse length
- wavelength
- fluence

But which of these dependencies are important and should be included into the model? As mentioned before, the wavelength and pulse length of the laser beam is assumed to be constant. Furthermore, the surface material is restricted to aluminium. So, we are only left with the angle of incidence, polarization and fluence which are not constant along the surface. For

the Laser-Based Debris Removal scenario the laser has to pass a turbulent atmosphere leading to a quite unpolarized beam. The influence on the results is furthermore only strong for shallow angle of incidence. But for such small angles, the energy of the beam is distributed over a larger area and the resulting $\Delta\vec{p}_D$ becomes rather small. Because of that, the polarisation and the angle of incidence are fixed too. The only dependency left is the fluence Φ. The variation of the fluence along the surface arises on the one hand from the varying fluence along the beam profile of the laser itself and on the other hand from the different incident angle of the beam on the surface. Therefore, we have to find an expression for $c_m(\Phi)$. Fortunately, the same model (Polly-2T) can be used to calculate the coupling coefficient c_m for different values of Φ, leading so to a characteristic shaped figure like the one in Figure 5. [13] One can see that the coupling

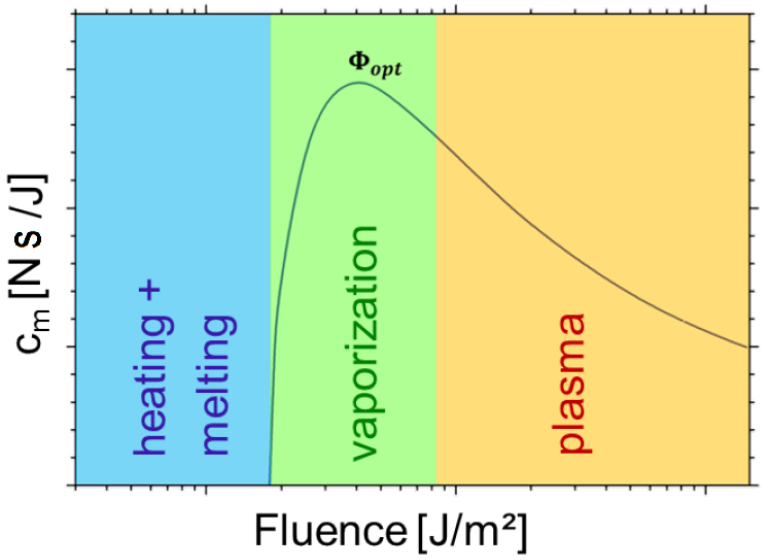

Figure 5: Characteristic behaviour of the coupling coefficient c_m for different fluence Φ. There are three regimes: the heating without ablation, the vaporization and the plasma shielding regime. Copyright: DLR

coefficient is zero below a certain limit, called the ablation threshold Φ_0. For higher fluences, ablation is occurring but the coefficient is only raising to a certain maximum. If the fluence is too high, the formed plasma jet absorbs the incoming laser light (which is called plasma shielding) and the coupling coefficient is falling again. Note, that the resulting $\Delta\vec{p}$ is still raising as long as the incident energy is increasing. Because it would not be very performant to use Polly-2T to recalculate c_m again and again, one can use the analytical fitting function from [13]

$$c_m(\Phi) \approx \frac{\Phi - \Phi_0}{a + (\Phi - \Phi_0)} \cdot b \cdot 12.46 \cdot a_\mu^{7/16} \cdot \left(\frac{\sqrt{\tau}}{\lambda \cdot \Phi}\right)^c \quad . \tag{1.22}$$

This model leads to different curves for various materials and laser parameters. The material dependent fitting parameter are the ablation limit Φ_0 and three parameter a, b, c which have no further physical interpretation. The laser dependent parameter is the wavelength λ and the pulse duration τ. With the fluence dependent coupling coefficient Equation (1.21) and a variable surface normal $\hat{n}$ this leads to an expression which corresponds to the momentum per surface area induced at each point on the particle surface

$$\frac{d\vec{p}}{dA} = -c_m(\Phi') \cdot \Phi' \cdot \hat{n} \quad . \tag{1.23}$$

Note that Φ' is the fluence at a specific point on the targets surface and must be distinguished from the laser fluence Φ. The total momentum can be achieved by an integration over the illuminated target surface A

$$\Delta\vec{p} = \int_A \frac{d\vec{p}}{dA} dA = -\int_A c_m(\Phi') \cdot \Phi' \cdot \hat{n} \cdot dA \quad . \tag{1.24}$$

The momentum $\Delta\vec{p}$ is proportional to the illuminated surface A. Remembering Equation (1.10) and using the fact that the debris mass m_D is proportional to the particle volume v_D, one can find that the change in debris velocity is $\Delta\vec{v} \propto \frac{A}{m_D}$. This means, that the resulting change in velocity is proportional to the area mass ratio of the target. The mass of thin plates scales quadratic with the debris size d_D. The resulting change in velocity $\Delta\vec{v} \propto \frac{A}{m_D} \propto \frac{d_D^2}{d_D^2} = 1$ is so independent of the actual size. But for voluminous objects, for example a sphere, one can get $\Delta\vec{v} \propto \frac{1}{d_D}$ which restricts the feasible use of this method to small debris sizes.

1.3 Momentum Generation at Complex Target Geometries

In the following, two methods are introduced for calculating $\Delta\vec{p}$ based on Equation (1.24). The first one is an analytical description. The second is a numerical approach, which will be used in the following chapters.

1.3.1 Analytical Description: Area Matrix Approach

One approach to actually calculate the generated momentum is the area matrix approach introduced in [14] and further explained in [11]. It is based on a discretisation of the target objects surface and so to a discretisation of the integral in Equation (1.24)

$$\Delta\vec{p} = \sum_{i=1}^{N} \Delta\vec{p}_i = -\sum_{i=1}^{N} c_m(\Phi'_i) \cdot \Phi'_i \cdot \hat{n}_i \cdot A_i \quad . \tag{1.25}$$

The surface of the target object which is directed to the laser is split into N flat components denoted with index i. The form is unimportant but the area A_i and the orientation $\hat{n}_i$ has to be known. To get a simple analytical solution, the coupling coefficient is assumed to be constant $c_m(\Phi'_i) = c_m = const.$ and a constant laser fluence $\Phi = const.$ is chosen. Because the surface can be tilted with respect to the laser direction $\hat{k}$, one has to calculate the target fluence Φ' which is actually reaching the surface of the target (Due to the tilting, the energy is distributed over a larger area and so the energy area density is decreased.)

$$\Phi'_i = \Phi \cdot \cos\alpha_i = -\Phi \cdot \hat{k} \cdot \hat{n}_i \tag{1.26}$$

α_i is the angle between surface normal and laser direction. In Equation (1.25) this leads to a change in momentum induced by each single section i

$$\Delta\vec{p}_i = c_m \Phi A_i (\hat{k} \cdot \hat{n}_i) \hat{n}_i \quad . \tag{1.27}$$

The total momentum induced by the pulse can then be calculated by summation over all surface elements

$$\Delta\vec{p} = \sum_{i=1}^{N} \Delta\vec{p}_i \tag{1.28}$$

$$= c_m \Phi \sum_{i=1}^{N} A_i (\hat{k} \cdot \hat{n}_i) \hat{n}_i \quad . \tag{1.29}$$

This formula can then be rewritten in matrix form. For each component $l = 1,2,3$ of $\Delta\vec{p}$ one can write

$$\Delta\vec{p}_l = c_m \Phi \sum_{i=1}^{N} \sum_{j=1}^{3} \hat{k}_j \hat{n}_{ji} A_i \hat{n}_{il} \tag{1.30}$$

$$= c_m \Phi \sum_{j=1}^{3} \hat{k}_j \sum_{i=1}^{N} \hat{n}_{ji} A_i \hat{n}_{il} \quad . \tag{1.31}$$

The last part can be rewritten as a matrix which only depends on the orientation and area of the i surface elements

$$\mathbf{G}_{lj} = \sum_{i=1}^{N} \hat{n}_{il} A_i \hat{n}_{ij} \quad . \tag{1.32}$$

The expression for $\Delta\vec{p}$ is now simply a matrix vector multiplication with the 'Area Matrix' and the laser direction $\hat{k}$ times laser fluence and coupling coefficient

$$\Delta\vec{p} = c_m \Phi \mathbf{G} \hat{k} \quad . \tag{1.33}$$

1.3.2 Numerical Discretization for Irregularly Shaped Targets

Although the area matrix approach provides an easy tool to calculate the momentum generation on an object, it has several drawbacks:

- the coupling coefficient c_m is assumed to be constant
- self-shadowing of the geometry is neglected, leading to incorrect results for complex geometries
- constant fluence profile is assumed

If one wants to investigate the behaviour of an arbitrarily shaped space debris under pulsed irradiation, this approach is clearly insufficient. To solve these problems, a new numerical method was developed in [3], using a raytracing approach. In the following, a short overview of this method is given. The main concept is to handle the laser beam according to geometrical optics which allows it to cut the beam into same sized rays, each of them assumed to have a quadratic profile. With a lattice size h_L and an overall beam size d_L this leads to $N = (\frac{d_L}{h_L})^2$ rays, indexed with i. Because a pulsed laser is used, the beam profile can be described by the time independent fluence distribution $\Phi(\vec{x})$, which can now be attached to the rays Φ_i according to the position of the rays relative to the beam centre. This profile can principally follow an arbitrary distribution. Despite this, the distribution is restricted to constant and Gaussian profiles in the original code.

The aim of the method is now to calculate the change in momentum $\Delta\vec{p}$ and angular momentum $\Delta\vec{L}$. To use Equation (1.25) one must find a way to transfer the rays and laser fluence to the target surface. To do so, we perform a projection via ray-tracing. The code is able to calculate the closest intersection of the rays with a few analytical geometries as well as arbitrary models, provided by a triangle mesh. This meshes can be designed, for example, with a CAD program like Solid Edge. The two interesting results of this calculation are the position of the hit $\vec{x}_{hit}$ and the normal vector of the intersected surface/triangle $\hat{n}_{hit}$. Like in the Area Matrix Approach we must pay attention to the tilting of the surface relative to the laser beam. The target fluence is again $\Phi_i' = \Phi_i \cdot \cos\alpha_i$. The surface area is also effected in this way $A_i = \frac{h_L^2}{\cos\alpha_i}$ leading to

$$\Delta\vec{p} = \sum_{i=1}^{N} \Delta\vec{p}_i = -\sum_{i=1}^{N} c_m(\Phi_i \cdot \cos\alpha_i) \cdot \Phi_i \cdot \cos\alpha_i \cdot \frac{h_L^2}{\cos\alpha_i} \cdot (\hat{n}_{hit})_i \tag{1.34}$$

$$= -\sum_{i=1}^{N} c_m\left(-\Phi_i \cdot \hat{k} \cdot (\hat{n}_{hit})_i\right) \cdot \Phi_i \cdot h_L^2 \cdot (\hat{n}_{hit})_i. \tag{1.35}$$

The surface normal vector gives the direction of the induced momentum. The absolute value is defined by the coupling coefficient $c_m(\Phi_i')$ multiplicated with the energy of ray i. With the momentum, one can simply calculate the angular momentum of ray i by a cross product with the position of the hit

$$\Delta\vec{L} = \sum_{i=1}^{N} \Delta\vec{L}_i = \sum_{i=1}^{N} (\vec{x}_{hit})_i \times \Delta\vec{p}_i. \tag{1.36}$$

To get an angular momentum which is referred to the centre of mass, the object data should be given in centre of mass (CMS) coordinates.

2 Modelling of Laser-Based Debris Removal

2.1 Introduction

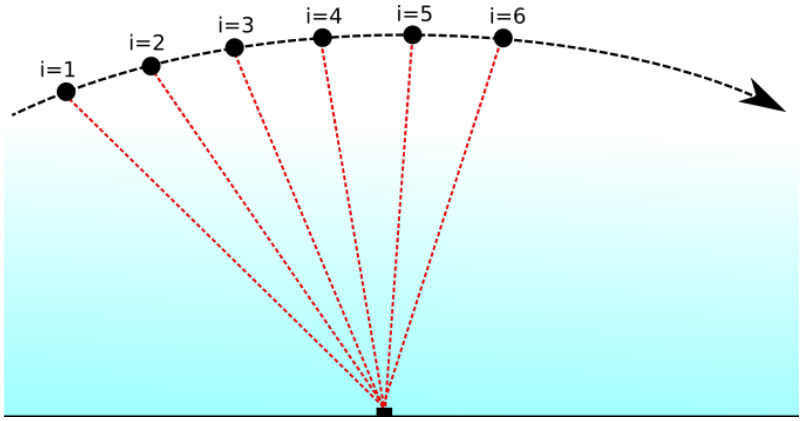

Figure 6: The transit is discretized into several steps i, sending a pulse at each step and propagating in between.

To evaluate the efficiency of this removal method, it is essential to find an appropriate model to calculate the resulting change in orbit induced by an illuminated transit. With this, one could investigate if the orbit is lowered, leading so to an earlier re-entry. Furthermore, one wants to eliminate the danger of an uncontrolled debris particle which could eventually harm a satellite, or even worse, a manned spaceship. To do this, a model was designed which is able to calculate the new orbit of one single debris particle after one transit under repetitively pulsed laser irradiation. A single laser station at a fixed position is assumed which results in a laser beam with the parametrization introduced in Section 1.2. The station position is saved in the "earth-centered, earth-fixed" (ECEF) frame which is like the "earth-centered inertial" (ECI) frame originated in the center of the Earth but in contrast to later rotating with the surface of the earth (See Section 2.2.1). Note, that the laser beam is heavily effected by several uncertainties caused by instrumentation issues at the station and by atmospheric perturbation. The fluence distribution will be assumed to be Gaussian at the target object and we will only pay attention to perturbations on the laser beam direction. The model of this behaviour will be discussed in more detail in Section 2.2.2. As criteria for switching the laser on or off, the elevation $\tilde{\epsilon}$ introduced in Section 2.3 is used. This means the simulation is initiated, when the target object reaches the start elevation $\tilde{\epsilon}_s$ and terminates when it reaches the ending elevation $\tilde{\epsilon}_e$. The time t between this two points is discretized into time steps $i \in [0, N]$, leading to a simulation time of

$$t_i = i \cdot h \tag{2.1}$$

with a step size h. The laser pulse and the ablation process is assumed to be instantaneous. Because the repetition rate f is constant, pulse i can be send exactly when $t = t_i$ which leads to a natural choice for the step size $h = \frac{1}{f}$.

The debris particle surface will be restricted to only one single surface material and therefore one set of laser matter interaction parameter. The shape, mass m_D and the inertia tensor $\mathbf{J}$ are so sufficient to fully describe the target particle. This is closer discussed in Section 2.4.1. Also note, that we assume that the geometry is fixed during the transit. This is important to say, because the interaction with the laser leads to ablation of material and so to a change of the surface. Nevertheless, these changes are typically sub-micrometer per laser pulse that they are

neglected in this model. To fully describe the dynamics of the particle, one has to take care of the position at each time point t_i during the simulation. Because the orientation of the particle is heavily affecting the outcome of the ablation process, the rotation is also included into the calculation:

- position $\vec{x}_i$
- momentum $\vec{p}_i$
- orientation $\mathbf{R}_i$
- angular momentum $\vec{L}_i$

So, one has to propagate the position, momentum and the orientation from time step i to $i+1$. The position and momentum will be calculated by the propagator introduced in Section 2.4.2 and the rotation by the propagator introduced in Section 2.4.3 leading to a change in position $\Delta\vec{x}_G$ and momentum $\Delta\vec{p}_G$ which is caused by the gravitation of the earth. The rotation propagator leads to an operator $\Omega : SO(3) \to SO(3)$ which maps the orientation at time step i at the orientation at time step $i+1$. In total one gets four equations

$$\vec{x}_{i+1} = \vec{x}_i + \Delta\vec{x}_G\left(\vec{x}_i, \vec{p}_i\right) \tag{2.2}$$
$$\mathbf{R}_{i+1} = \Omega\left(\mathbf{R}_i, \vec{L}_i\right)\mathbf{R}_i \tag{2.3}$$
$$\vec{p}_{i+1} = \vec{p}_i + \Delta\vec{p}_G\left(\vec{x}_i, \vec{p}_i\right) \tag{2.4}$$
$$\vec{L}_{i+1} = \vec{L}_i \tag{2.5}$$

Up to this point only the movement of an undisturbed particle is described. To insert the interaction with the laser we want to use the laser matter interaction model introduced in Section 1.3.2. For each pulse, and so for each time step i, this leads to an additional ablation induced change in momentum $\Delta\vec{p}_A$ and angular momentum $\Delta\vec{L}_A$. The values at time step i should already include the effects of pulse i. This leads in total to

$$\vec{x}_{i+1} = \vec{x}_i + \Delta\vec{x}_G\left(\vec{x}_i, \vec{p}_i\right) \tag{2.6}$$
$$\mathbf{R}_{i+1} = \Omega\left(\mathbf{R}_i, \vec{L}_i\right)\mathbf{R}_i \tag{2.7}$$
$$\vec{p}_{i+1} = \vec{p}_i + \Delta\vec{p}_G\left(\vec{x}_i, \vec{p}_i\right) + \Delta\vec{p}_A\left(\vec{x}_{i+1}, \mathbf{R}_{i+1}\right) \tag{2.8}$$
$$\vec{L}_{i+1} = \vec{L}_i + \Delta\vec{L}_A\left(\vec{x}_{i+1}, \mathbf{R}_{i+1}\right) \tag{2.9}$$

In this way, the process can be integrated stepwise. With the equations in Section 1.1 one can finally calculate the change in orbit elements from the final position and velocity of the particle after the transit. The only open question is now the initial condition of the particle which consists of:

- initial position $\vec{x}_0$
- initial momentum $\vec{p}_0$
- initial orientation $\mathbf{R}_0$
- initial angular momentum $\vec{L}_0$

Position and momentum could be calculated analytical for circular orbits. If one wants to use real orbits given in the TLE Format, the included SGP4 model [15] can be used to calculate the initial position and momentum. Even if one can analyse light curves from space

debris observations we assume the orientation $\mathbf{R}_0$ to be generally unknown. For the angular speed ω_0 a rough assumption based on Section 1.1 is used. Although the direction of the rotation is unknown we can get an initial angular momentum with a random unity vector $\hat{n}$ with $\vec{L}_0 = \mathbf{J} \cdot (\omega_0 \cdot \hat{n})$.

2.2 Laser irradiation issues

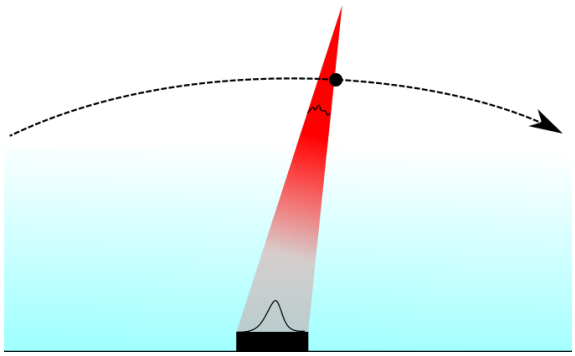

Figure 7: Illustration of the beam propagating through the atmosphere.

To calculate the interaction between the target object and the laser, one needs the position of the laser $\vec{x}_L$ and its direction $\vec{k}$. Furthermore, a beam profile/fluence distribution at the target is needed. Although the atmosphere and laser device leads to a varying profile at the target from pulse to pulse we assume a pulse independent profile $\Phi_i(\vec{x})$ in this thesis. Later on this could be replaced by a fully propagated beam but such a model would clearly exceed the scope of this thesis. If the profile is fixed, one has only take care for the direction of the laser $\vec{k}$ and the position of the laser station $\vec{x}_L$. The laser beam can then be defined by a straight line $\vec{x}_L + s \cdot \vec{k} \quad s \in (0, \infty)$. We do this although the beam is clearly not propagating as a straight line through the atmosphere but we can use the difference between laser position and the nearest intersection of the beam as $\vec{k}$. The angle between k and the apparent direction is called "angle of arrival". According to [16] this angle is in the μrad range, so we can neglect this effect and focus completely on the direction $\vec{k}$. In the following, the calculation of the position $\vec{x}_L$ and the pointing direction $\vec{k}$ are further discussed.

2.2.1 Surface Propagation

The coordinates of the laser station are saved in time-independent polar coordinates (longitude, latitude). To be able to use this position (e.g., for calculation of the aiming direction of the laser) the ECEF has to be 'propagated' to ECI, using the orientation of the earth at that moment. The time invariant position in ECEF coordinates is

$$x_{ECEF} = \begin{pmatrix} r_e \sin(\frac{\pi}{2} - \phi) \cdot \cos\Lambda \\ r_e \sin(\frac{\pi}{2} - \phi) \cdot \sin\Lambda \\ r_e \cos(\frac{\pi}{2} - \phi) \end{pmatrix}$$

with the longitude Λ, latitude ϕ and earth radius r_e. To get the time dependent position in ECI, x_{ECEF} has to be rotated around the rotation axis of the earth (here the z-axis) according to the actual orientation angle of the earth. This angle γ, which is called sidereal angle, can be described as a function of time. This relation is not part of the model and can later on easily

be calculated by using a function out of the astropy package [17]. The transformation matrix is then

$$T_{ECEF2ECI} = \begin{pmatrix} \cos\gamma & -\sin\gamma & 0 \\ \sin\gamma & \cos\gamma & 0 \\ 0 & 0 & 1 \end{pmatrix} \quad .$$

And finally the ECI position is given by

$$x_{ECI} = T_{ECEF2ECI} x_{ECEF} \quad . \tag{2.10}$$

2.2.2 Laser Aiming Accuracy

To get the aiming direction $\vec{k}$ of the laser, there are basically two different strategies:

- the laser is tracking the target
- the laser is aiming at the known orbit, without taking into account the change in orbit during the irradiation

As mentioned in [18, Ch. 4.2.2], the ablation process would cause the object to leave the laser beam quite fast, leading to a reduced efficiency of the whole method. Because of that, the first strategy is chosen for the following simulation. If it is assumed, that the position of the object at each point in time is exactly known, the aiming direction $\vec{k}$ of the laser is then simply the difference between laser position and the centre of mass of the debris object in ECI coordinates

$$\vec{k} = \vec{x}_D - \vec{x}_L \quad . \tag{2.11}$$

If one wants to simulate the second behaviour, it could easily be implemented by creating a second identical target and aiming at this dummy particle while shooting at the real one. How-

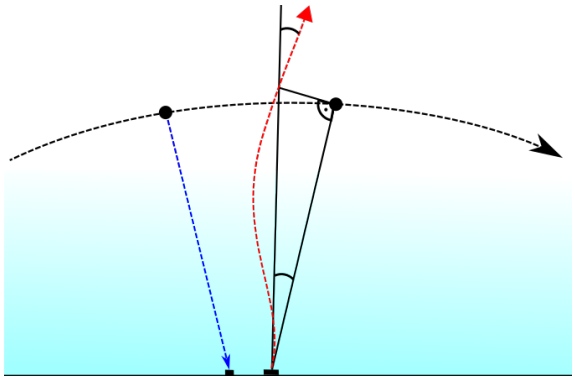

Figure 8: Illustration of pointing uncertainties. (a) errors in target tracing, (b) technical restrictions of the telescope, (c) atmospheric perturbations on the laser beam

ever, this direction is not a realistic assumption. Because of interferences like

- errors in target tracing
- technical restrictions of the telescope
- atmospheric perturbations (seeing)

the resulting aiming direction can only be known to a certain value. How could one model this behaviour? First we define a probability density function $P(\Delta k)$ which describes the probability that the centre of the beam misses the debris centre of mass by Δk. Because Δk depends on the distance, it seems advisable to use the pointing angle α at the laser station instead. We define, that for $\alpha = 0$ the beam is pointing directly at the debris centre of mass. With the distance to the target $l = |\vec{k}|$ we get

$$\Delta k = l \cdot \tan\alpha \approx l \cdot \alpha \quad . \tag{2.12}$$

The last estimate is a Taylor approximation, using that α is in magnitudes of μrad which will be shown in the following. We are looking now for an expression for $P(\alpha)$. We assume for $P(\alpha)$ an isotropic normal distribution which leads to a single parameter: σ

$$P(\alpha) = \frac{1}{2\pi\sigma^2} e^{-\frac{\alpha^2}{2\sigma^2}} \quad . \tag{2.13}$$

The plan is now to estimate the contributions of the single uncertainties to the total σ. First we have to know the tracking error σ_T which stands for the unknown position of the target. A method to measure the position of a space debris particle is given by imaging the object with a telescope while it is illuminated by the sunlight. This is done for example at the observatory in Stuttgart and leads to two angles in observer-centred spherical coordinates. The uncertainty of this process can be assumed to be $2\mu rad$ [19].

The second error is the pointing error of the laser σ_P which arises from electronic or mechanical restrictions of the sending telescope. This error can be estimated by literature values of already existing telescopes. For example, the pointing error of the Very Large Telescopes (VLT) at the Paranal Observatory in Chile is around $3 arcseconds$ RMS [20] and so $14\mu rad$. The Isaac Newton Group of Telescopes state $1.5 arcsec$ RMS ($7\mu rad$) [21]. The Cleanspace study itself proposes a pointing accuracy of $0.05 arcsec$ [22].

At last we need the alteration of the beam direction induced by the atmosphere σ_S. In the theory of laser communication systems, this effect is known as beam wander [16] and describes the spread in distance between beam centre and real target position. Because the physics is basically the same, we can use the uplink theory for our problem as well. The following formula for the standard deviation of the angular displacement is derived from the formula for the displaced RMS $\langle \Delta k^2 \rangle$ in [16, p. 523 Eq. 98]

$$\sigma_S = \frac{\sqrt{\langle \Delta k^2 \rangle}}{(H - h_0)\sec(\zeta)} = 0.73 \left(\frac{\lambda}{2W_0}\right)\left(\frac{2W_0}{r_0}\right)^{5/6} \tag{2.14}$$

ζ is the zenith angle, W_0 the beam diameter at the transmitting telescope, λ the wavelength of the laser beam, h_0 the height of the laser station (over sea level) and H the effective height which has to be seen as a kind of cut-off. Above this, the atmosphere is too thin and can be neglected. This obeys the weak turbulence theory developed in [16] which is applicable for small beam diameter up to a few centimetres. For larger beam diameter one should use the strong turbulence theory to pay attention to turbulences which are smaller than the beam and leads so to a further distortion within the beam cross-section. But because this theory needs further assumptions of the beam quality we use for the moment the week turbulence theory. The last open parameter r_0 is the so called fried parameter and defines a measure for the quality of the seeing. A definition can be found in [16, p. 492 Eq. 23]

$$r_0 = \left(0.42\sec(\zeta)\frac{4\pi^2}{\lambda^2}\int_{h_0}^{H} C_n^2(h)\,dh\right)^{-3/5} \quad . \tag{2.15}$$

Again there is the zenith angle ζ and the wavelength of the beam λ. Furthermore, it contains a integration over the atmospheric turbulence strength $C_n^2(h)$ which is heavily dependent on the height, time of day and weather. SLC Model which is a mean from measurements above mount Haleakala on Hawaii [16, p. 482 eq. 5]

$$C_n^2(h) \approx \begin{cases} 8.87 \cdot 10^{-7} \frac{1}{h^3}, & 1500m < h < 7200m \\ 2.0 \cdot 10^{-16} \frac{1}{\sqrt{h}}, & 7200m < h < 20000m \end{cases} \tag{2.16}$$

It is easy to see: if h_0 is larger, r_0 decreases and so does σ_S. So we have a motivation to put the laser station on a high mountain to reduce the error. This is also a reason why astronomical observatories are often on mountain tops. If one restricts the transit to near zenith which means $\zeta < 40°$ the dependency on the zenith can be neglected $\sec(\zeta) = \frac{1}{\cos(\zeta)} \approx 1$. The influence of the seeing is then independent of the debris position and leads so to a constant σ_S. Assuming a wavelength of $\lambda = 1064nm$ and a station height of $h_0 = 2600m$ will result in

$$\sigma_S(W_0) = 6.32543 \cdot 10^{-7} \cdot W_0^{-1/6} \quad . \tag{2.17}$$

According to [22] we choose $W_0 = 5m$ which leads to $\sigma_S = 0.4\mu rad$.
The final σ can now be calculated by a quadratic adding of the three uncertainty factors

$$\sigma^2 = \sigma_T^2 + \sigma_P^2 + \sigma_S^2 \quad . \tag{2.18}$$

This formula already requires that the three contributions are uncorrelated. This is obvious for σ_P but there could be a correlation between the path of the light which is taken for the tracking and the uplink path of the transmitted laser pulse. Because the target is moving, there is a difference angle between the observed position and the position to shoot at.

To get now an estimation, how often one can hit with a given σ and distance to the target l, a short analytical calculation is now delivered. The expectation value is defined by

$$\langle H \rangle = \int_{-\infty}^{\infty} \int_0^{\pi} H(\alpha) P(\alpha) |\alpha| d\phi d\alpha \tag{2.19}$$

$$= \pi \int_{-\infty}^{\infty} H(\alpha) P(\alpha) |\alpha| d\alpha \tag{2.20}$$

with an integration over α and the polar orientation ϕ around k. $H(\alpha)$ is a function which is equal to one when there is a hit with α, zero when not. Because the debris diameter d_D is much smaller than the laser diameter d_L the debris is assumed to be just a point without spatial extend. A hit is then the case if $\Delta k = l \cdot \alpha \leq \frac{d_L}{2}$ leading to

$$H(\alpha) = \begin{cases} 1, & |\alpha| \leq \frac{d_L}{2l} \\ 0, & |\alpha| > \frac{d_L}{2l} \end{cases} \quad . \tag{2.21}$$

Inserting this expression in Equation (2.20) effects simply the integral limits and results into

$$\langle H \rangle = \pi \int_{-\infty}^{\infty} H(\alpha) P(\alpha) |\alpha| d\alpha \tag{2.22}$$

$$= \pi \int_{-\frac{d_L}{2l}}^{\frac{d_L}{2l}} P(\alpha) |\alpha| d\alpha \tag{2.23}$$

$$= 2\pi \int_0^{\frac{d_L}{2l}} P(\alpha) \alpha d\alpha \tag{2.24}$$

$$= 1 - e^{-\frac{d_L^2}{8l^2\sigma^2}} \tag{2.25}$$

.

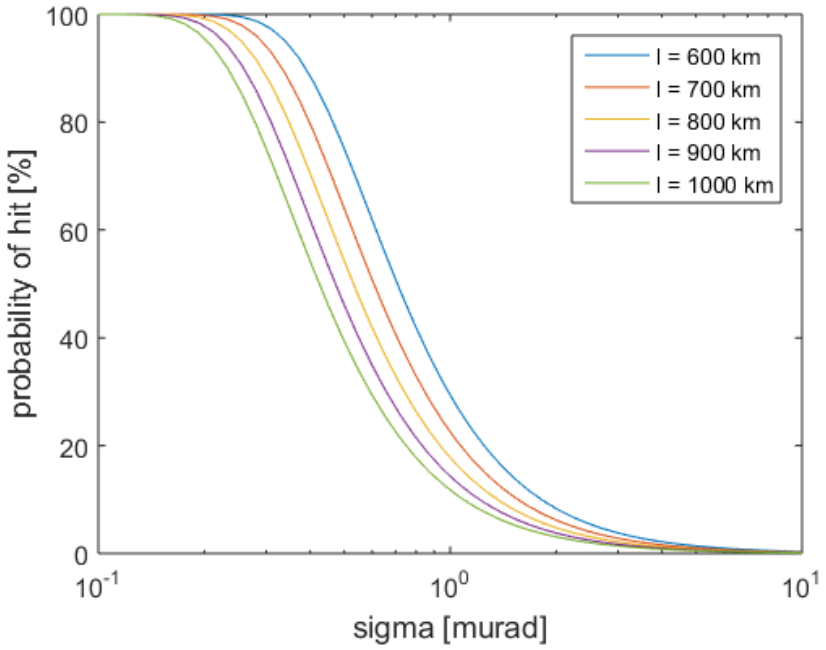

Figure 9: Plot of the hit probability over σ for different distances l using Equation (2.25)

One can so finally estimate, that one need at least an aiming accuracy of $\sigma = 4\mu rad$ to bring 1 of 100 pulses at the target.

To model the probability density function, an angle α is chosen randomly centred at 0 with an standard deviation of σ. To avoid unphysical behaviour, we introduce a cut-off for angles $|\alpha| > 10^{-3} rad$. Afterwards the aiming error at the target is calculated via

$$\Delta k = |\vec{k}| \cdot \tan\alpha \quad . \tag{2.26}$$

The randomized direction $\vec{k}_\sigma$ is then given by

$$\vec{k}_\sigma = \vec{k} + \Delta k \cdot \vec{t} \tag{2.27}$$

where $\vec{t}$ is a random unity vector orthogonal to k which ensures, that no direction is favoured.

2.3 Laser Switching Criterion

One still needs a criterion when to turn the laser on or off. For this we simply use the apparent elevation of the target, seen from the laser station. If the target reaches the start elevation e_s the laser is switched on until the object reaches an end elevation e_e to be defined. The elevation is defined as the angle between the horizon and the apparent position of an object seen from the observer. An object at the horizon has the angle 0. An object at the zenith has an elevation of $\pi/2$. Let now $e : [t_s, t_e] \rightarrow [0, \frac{\pi}{2}]$ be the elevation of an object as function of the simulation time. We want to use the elevation as criterion for switching the laser on or off. This is causing a problem, because according to this definition the elevation is not injective. The elevation of an object will rise to its maximum and decline afterwards to the horizon. This means, that every elevation $e < e_{max}$ will be reached twice during a transit. This problem makes a new injective definition $\tilde{e}$ of the elevation necessary, using the fact that the elevation of a satellite has only one extremum (maximum) during a transit. With $t_z = \arg\max(e(t))$ this allows us to split the transit into a phase with increasing elevation $[t_s, t_z]$ and a phase with decreasing elevation $(t_z, t_e]$. We can now define a new function which plots the decreasing phase to the interval $(\pi/2, \pi]$. So it follows that

$$\tilde{e} : [t_s, t_e] \rightarrow [0, \pi] \tag{2.28}$$

with

$$\tilde{e}(t) = \begin{cases} e(t), & t \leq t_z \\ \pi - e(t), & t > t_z \end{cases} . \tag{2.29}$$

It is easy to see, that this function is injective because the increasing phase is mapped to $[0, \pi/2]$ and the decreasing phase to $(\pi/2, \pi]$. In the following, a short explanation is given how the calculation of the elevation is done by the simulation at a specific point of time. Let $\hat{k}$ be the normalized laser direction vector from Section 2.2.2. Furthermore, let $\vec{t}_1$ and $\vec{t}_2$ be the unity vectors defining the plane tangential to the earth's surface at the laser position. The elevation e is then calculated by projecting $\hat{k}$ on the tangential plane and measuring the angle between the projection $\vec{p}$ and $\hat{k}$

$$\vec{p} = (\hat{k} \cdot \vec{t}_1)\vec{t}_1 + (\hat{k} \cdot \vec{t}_2)\vec{t}_2 \tag{2.30}$$

$$e = \arccos(\hat{k} \cdot \vec{p}) \quad . \tag{2.31}$$

From e, $\tilde{e}$ can easily be obtained by Equation (2.29). To find out if the object is in the increasing or decreasing phase at the moment of calculation, a vector $\vec{u}$ is defined which is standing orthogonal on $\vec{k}$ and pointing upwards, away from the earth surface. If the orbital velocity is pointing in the same direction as this vector, the elevation is increasing. Otherwise its decreasing

$$\tilde{e} = \begin{cases} e, & \vec{v} \cdot \vec{u} \geq 0 \\ \pi - e, & \vec{v} \cdot \vec{u} < 0 \end{cases} . \tag{2.32}$$

2.4 Space debris issues

2.4.1 Material and Geometry

One needs the mass m_D and the inertia tensor $\mathbf{J}$ of a particle to connect the angular and translational momentum, which were calculated by Expedit with the dynamic quantities:

$$\vec{p} = m_D \cdot \vec{v} \tag{2.33}$$

$$\vec{L} = \mathbf{J} \cdot \vec{\omega} \quad . \tag{2.34}$$

Because one would like to vary material and geometry of the target object independently, the mass m_D and the inertia Tensor $\mathbf{J}$ are a problematic input because both are depending on the material as well as on the geometry. To do this, both are split into pure geometry-related and material-related parameter. Each particle is assumed to consist of only one material. Therefore, the density is independent from the position $\vec{r}$ of the infinitesimal volume element dV

$$\rho(\vec{r}) = \begin{cases} \rho_0, & \vec{r} \in \mathbf{V}_D \\ 0, & \vec{r} \notin \mathbf{V}_D \end{cases} \quad . \tag{2.35}$$

So the mass can be trivially split by writing

$$m_D = \int_V \rho(\vec{r}) dV = V \cdot \rho_0 \quad . \tag{2.36}$$

Using now the integral definition of the inertia tensor for arbitrary formed bodies [23, p.85], the density of the particle ρ_0 can be extracted

$$\mathbf{J}_{ij} = \int_V (\vec{r}^2 \delta_{ij} - \vec{r}_i \vec{r}_j) \rho(\vec{r}) dV \tag{2.37}$$

$$= \rho_0 \int_V (\vec{r}^2 \delta_{ij} - \vec{r}_i \vec{r}_j) dV \tag{2.38}$$

$$= \rho_0 \cdot \mathbf{J'}_{ij} \tag{2.39}$$

with the indices $i, j \in [1,3]$. $\mathbf{J'}$ is the normalized inertia tensor

$$\mathbf{J'}_{ij} = \int_V (\vec{r}^2 \delta_{ij} - \vec{r}_i \vec{r}_j) dV \quad . \tag{2.40}$$

Again, the expression for the new defined inertia tensor in Equation (2.40) only depends on the geometry of the object. Normalized means, that the tensor is calculated with a density of $\rho = 1$. Summarizing, a geometry is described by

- volume V
- normalized inertia tensor $\mathbf{J'}$ in CMS
- triangle positions in CMS describing the actual geometry

and a material can be described by

- density ρ
- laser matter interaction parameter $a, b, c, x_0, a_\mu, \lambda, \tau$

The actual debris can be composed out of a geometry and a material. Note, that the LMI parameter are dependent on the laser, too. So, a suitable set of parameters has to be chosen according to the settings of the laser for λ and τ.

2.4.2 Orbital Propagation

For an exact propagation of objects in space, attention must be paid to several factors like:

- Atmospheric drag
- Radiation pressure
- Gravitation of several bodies
- Inhomogeneous gravitation field

However, transit times for this problem are short (few minutes) and the mass of the debris small that it seems to be sufficient to approximate the orbit with an simple Newtonian approach, neglecting all factors except the gravitation force of the earth which is be assumed to be homogeneous and therefore only depending on the distance of an object to the earth centre. Using Newton's law of universal gravitation

$$\vec{F}_{grav} = -\frac{\mu m_D}{\vec{x}^2}\frac{\vec{x}}{|\vec{x}|} \tag{2.41}$$

where $\vec{x}$ is the vector from earth center to the object center and m_D the mass of the object. Using then the second Newtonian law $\vec{F} = m_D \cdot \vec{a}$ one can get the acceleration on an object at position $\vec{x}$ in ECI and time t with

$$\vec{a}(t) = -\frac{\mu}{(\vec{x}(t))^2}\frac{\vec{x}(t)}{|\vec{x}(t)|} \quad . \tag{2.42}$$

With an step size Δt we can numerically integrate this acceleration over time via the velocity verlet algorithm [24], performing the following 3 steps in a loop:

$$\vec{v}(t+\frac{1}{2}\Delta t) = \vec{v}(t) + \frac{1}{2}\vec{a}(t)\Delta t \tag{2.43}$$

$$\vec{x}(t+\Delta t) = \vec{x}(t) + \vec{v}(t+\frac{1}{2}\Delta t)\Delta t \tag{2.44}$$

$$\vec{v}(t+\Delta t) = \vec{v}(t+\frac{1}{2}\Delta t) + \frac{1}{2}\vec{a}(t+\Delta t)\Delta t \quad . \tag{2.45}$$

But how is it possible to insert this into the time discretisation introduced in Section 2.1? There, we have a timestep h which is also defined as the time between two shoots $h = \frac{1}{f}$. But what will happen if the user chooses a quite low repetition rate? The timestep would become large and the error of the numerical integration unsatisfyingly big. So, there is an additional discretisation between the timesteps i and $i+1$ in simulation time. Introducing a timestep for the orbital propagator $h_{orbit} < h$ we can define the number of intermediate steps with $N_j = \frac{h}{h_{orbit}}$ and so an integration timestep $\Delta t = \frac{h}{N_j}$. Starting with the values at t_i we can run it in a loop N_j times and finally using the result as new values for step $i+1$. To ensure, that N_j is an integer, it is always rounded up to the nearest integer. Therefore, it follows that if $h_{orbit} > h$ the stepsize for the propagator equals the simulation timestep $\Delta t = h$. Because this is the direct numerical solution of the Kepler problem, it has the additional advantage, that one can use the analytical formula introduced in Section 1.1 to directly calculate the orbital elements from the velocity and position of the object at every step.

2.4.3 Rotation Propagation

An important aspect of the total simulation is the rotation of the debris. The orientation of the target is a major influence on the resulting change in momentum and angular momentum (See results in [3]). Starting with an orientation $\mathbf{R}(t)$ and an angular momentum $\vec{L}(t)$ at a specific point in time t, one must find a way to calculate the new orientation $\mathbf{R}(t')$ for $t' > t$. To do this, the angular velocity $\vec{\omega}$ can be calculated via

$$\vec{\omega}(t) = \mathbf{I}^{-1}\vec{L}(t) \tag{2.46}$$

with $\mathbf{I}$ as the inertia tensor of the object in ECI coordinates. As mentioned in Section 2.4.1, the inertia tensor $\mathbf{J}$ is saved in CMS coordinates. To get the inertia tensor in ECI coordinates it has to be rotated, using the rotation matrix $\mathbf{R}$

$$\mathbf{I} = \mathbf{R}\mathbf{J}\mathbf{R}^T \quad . \tag{2.47}$$

With $\vec{\omega}$ the new orientation can then be achieved by rotating $\mathbf{R}(t)$ by an angle of $|\vec{\omega}|(t'-t)$ around $\vec{\omega}$. For small $\Delta t = t' - t$ this may be true, but for larger Δt the dependency of $\mathbf{I}$ on the orientation $\mathbf{R}$ should be respected. This leads to a time discretized numerical approach. To gain the needed accuracy under reasonable computation costs a 3^{rd} order method is used [25, p. 388]. At each step i the inertia tensor has to be transformed to ECI coordinates with the actual orientation.

$$\mathbf{I}_i = \mathbf{R}_i\mathbf{J}_i\mathbf{R}_i^T$$

Afterwards a mean angular velocity $\vec{\omega}_{mean}$ is calculated with

$$\vec{\omega}_i = \mathbf{I}_i^{-1}\vec{L}_i \tag{2.48}$$

$$\dot{\vec{\omega}}_i = \mathbf{I}_i^{-1}(\dot{\vec{L}}_i - \vec{\omega}_i \times \vec{L}_i) \tag{2.49}$$

$$\ddot{\vec{\omega}}_i = \vec{\omega}_i \times \dot{\vec{\omega}}_i + \mathbf{I}_i^{-1}(\ddot{\vec{L}}_i - \dot{\vec{\omega}}_i \times \vec{L}_i - 2\vec{\omega}_i \times \dot{\vec{L}}_i + \vec{\omega}_i \times (\vec{\omega}_i \times \vec{L}_i)) \tag{2.50}$$

$$\vec{\omega}_{mean} = \vec{\omega}_i + \frac{\Delta t}{2}\dot{\vec{\omega}}_i + \frac{(\Delta t)^2}{6}\ddot{\vec{\omega}}_i + \frac{(\Delta t)^2}{12}((\dot{\vec{\omega}}_i + \frac{\Delta t}{3}\ddot{\vec{\omega}}_i) \times \vec{\omega}_i) \quad . \tag{2.51}$$

Because the rotation is only calculated between two shots and no interactions but the gravitational force during this time are assumed, the angular momentum is constant, i.e., $\dot{\vec{L}} = \ddot{\vec{L}} = 0$. The final integration step is than

$$\vec{\omega}_i = \mathbf{I}_i^{-1}\vec{L}_i \tag{2.52}$$

$$\dot{\vec{\omega}}_i = \mathbf{I}_i^{-1}(-\vec{\omega}_i \times \vec{L}_i) \tag{2.53}$$

$$\ddot{\vec{\omega}}_i = \vec{\omega}_i \times \dot{\vec{\omega}}_i - \mathbf{I}_i^{-1}(\dot{\vec{\omega}}_i \times \vec{L}_i - \vec{\omega}_i \times (\vec{\omega}_i \times \vec{L}_i)) \tag{2.54}$$

$$\vec{\omega}_{mean} = \vec{\omega}_i + \frac{\Delta t}{2}\dot{\vec{\omega}}_i + \frac{(\Delta t)^2}{6}\ddot{\vec{\omega}}_i + \frac{(\Delta t)^2}{12}((\dot{\vec{\omega}}_i + \frac{\Delta t}{3}\ddot{\vec{\omega}}_i) \times \vec{\omega}_i) \quad . \tag{2.55}$$

The new orientation can then be achieved by rotating $\mathbf{R}_i$ by an angle of $|\vec{\omega}|\Delta t$ around $\vec{\omega}_{mean}$.

$$\mathbf{R}_{i+1} = \Omega_{\vec{\omega}_{mean}}\mathbf{R}_i \quad . \tag{2.56}$$

Like the orbital propagator in Section 2.4.2, the integration is using an additional timestep $h_{orb} < h$ which was inserted in the same way.

2.5 Monte-Carlo Studies

As mentioned in Section 1.1, the final orbit is fully determined by the position and velocity after the last pulse. Because there is a sensible dependency on boundary conditions which are naturally unknown like

- orientation of the particle
- rotational speed of the particle
- material and geometry of the particle
- aiming accuracy of the laser

each transit results in a different orbit. So average values and standard deviation of the changed orbital elements are of interest. If we understand the model as a function $f_x : P \to \mathbb{R}$ which maps the boundary conditions (that means the phase space P) on the resulting value of a specific property after the transit, one can calculate the mean of this element, like for example the position, with

$$\langle \vec{x} \rangle = \frac{\int_P f_x(p) dp}{\int_P dp} \quad . \tag{2.57}$$

Because we would have to integrate over the whole phase space, which is continuous and would therefore cause infinite computation cost, a Monte Carlo approach is used. This means, that the integral is approximated by a finite sum over random points $p_l \in P$

$$\langle \vec{x} \rangle = \frac{\sum_{l=1}^{M} f_x(p_l)}{M} \quad . \tag{2.58}$$

In the following table, a short summation of the various uncertainties is given

Uncertainty	Distribution	Population
Laser Direction	Normal	$[\pm 10^3]\mu rad$
Initial Orientation	Uniform	$SO(3)$
Initial Rotation	Uniform	$\vec{\omega} \in \mathbb{R}^3$ with $\lvert\vec{\omega}\rvert = \omega_0$

Hence, P is given by a random combination out of these three populations according to the respective distributions plus the exact known boundary conditions introduced in 2.1. One would ask now: Why have we not included the uncertainty in debris material and geometry? Because it is hard to define a population for material and geometry. One could only try to use a few single representative combinations and try to calculate values for them, but the results would be only valid for this chosen combination. So in this thesis material and geometry are fixed in each Monte Carlo simulation, which allows to get the combined results via weighted averages afterwards. With the number of configurations Q and weights ω_r of configuration r one can get [26]

$$\langle x \rangle = \frac{\sum_{r=1}^{Q} \omega_r \langle x \rangle_r}{\sum_{k=1}^{Q} \omega_r} \tag{2.59}$$

$$\sigma_x^2 = \frac{\sum_{r=1}^{Q} \omega_r \left(\sigma_x^2\right)_r}{\sum_{k=1}^{Q} \omega_r} \quad . \tag{2.60}$$

Now the last question is, how many samples N do we need to approximate the integral in Equation (2.57) with the sum in Equation (2.58)? We know that we can get the integral as limit for

$N \to \infty$. But of course, we have to restrict ourself to a finite number. So there is one important question: How many steps are enough? Because we are using only rough estimates for the beam profile and the debris shapes, it seems to be reasonable to get estimates of the change in perigee up to a few hundred meters. With the formula introduced in Section 1.1, one can propagate this error back to the position $\frac{|\Delta\vec{x}|}{|\vec{x}|} < \epsilon_0$ and velocity $\frac{|\Delta\vec{v}|}{|\vec{v}|} < \epsilon_0$. One can now test the average value of the position $\vec{x}_N$ and velocity $\vec{v}_N$ on convergence and use ϵ_0 as error bound. This is done by calculating an estimation of the confidence interval of these values and comparing it to ϵ_0 [27]. This leads to

$$z_{\left(\frac{1+\beta}{2}\right)} \cdot \frac{\sigma^2}{\sqrt{M}} < \epsilon_0 \tag{2.61}$$

in which z is the quantil function of the normal distribution, σ^2 the estimated variance of the quantity and N the total number of samples. If this condition is true, β percent of the Monte Carlo simulations with M samples predict a mean which lies within an error of $\pm\epsilon_0$ to the real mean $\langle\vec{x}_N\rangle$ and $\langle\vec{v}_N\rangle$. $1-\alpha$ is the confidence level and is set to 95%. As 'emergency stop', a maximum number of steps M_{max} can be set. If the step number $l > M_{max}$ the simulation will stop and throw a 'no convergence' error.

3 Numerical Developments on laser-matter-interaction (LMI) simulations with Expedit

3.1 Introduction

After talking about the model, some details about the implementation are introduced in the following. Like mentioned in the introduction in Section 1.3.2 the LMI module ("EXPEDIT") was already implemented in the precursor thesis by Jascha Wilken. Thus, it seems rational to use this for the calculation of the interaction between the laser and the target. Because the original serial implementation was to slow for our Laser-Based Debris Removal scenario, the module was completely rewritten and improved in some points. First, the possibility was added to use arbitrary beam profiles. Further on, NVIDIA CUDA/Optix was used to severely increase the performance and an application programming interface (API) was created to enable the use of Expedit in python written codes. Additionally, the program was reduced to function as a pure laser matter interaction module, thus reducing code complexity and making it easier to use. For performance reasons, the program itself was written in C++ and CUDA C.

3.2 Customized beam profiles

The original software provides only the use of constant and Gaussian laser profiles. Because of device based aberration and atmospheric perturbations such ideal profiles differ a lot from real profiles. Thus, the possibility to use arbitrary laser profiles, like profiles calculated by at-

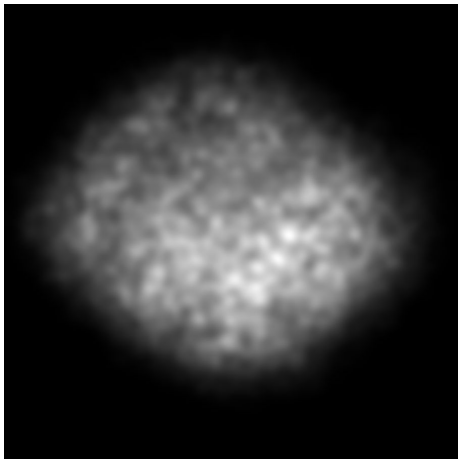

Figure 10: Laser profile measured during ablation experiments in Darmstadt (Refer to Section 5.2 for further details). The grey value of each pixel is proportional to the laser intensity at that specific point.

mospheric laser propagation simulations or measured in experiments, was added. The profile can now be forwarded to EXPEDIT as a 2D float array, called fluence map. It is a simple $N \times N$ grey scale image of the fluence distribution in which each pixel stands for a single ray with the fluence Φ_{ij} corresponding to the value of the pixel at position ij. As additional input the laser diameter d_L is needed. The profile can then be rescaled and placed in the scene with the centre of the fluence map at the laser position $\vec{x}_L$. With the resulting beam resolution $h_L = \frac{N}{d_L}$, this already defines the overall energy of the shot by summing up over all pixel values, which

corresponds to a discrete integration of the fluence over the laser profile

$$E_L = \int_A \Phi(\vec{x})\, dA = \sum_{i=0}^{N} \sum_{j=0}^{N} \Phi_{ij} h_L^2 \quad . \tag{3.1}$$

For the experimental validation in Section 5.2, a laser profile like the one in Figure 10 was used. This was obtained by splitting the laser beam and redirecting a weak image of the profile on a plate, prepared with a thermal paper (TSC in Figure 16). After each shot, a picture of the so generated image was taken. It can be assumed, that the value s_{ij} of the pixel at position ij is proportional to the fluence Φ_{ij}

$$\Phi_{ij} = c \cdot s_{ij} \quad . \tag{3.2}$$

If the energy of the laser is known, e.g., from measurements with a calorimeter, Equation (3.1) can be applied to calculate c by shifting the fluence to the desired energy

$$c = \frac{E_L}{E_S} = \frac{E_L}{\sum_{n=0}^{N} \sum_{m=0}^{N} s_{nm} h_L^2} \quad . \tag{3.3}$$

This means we are first normalizing the "pixel energy" E_S to one and multiply afterwards with the wanted laser energy E_L. The resulting map is then containing the correct profile and overall energy.

3.3 Improved Raytracing

A problem with the former code version is the simple implementation of the raytracing, which is basically a loop over all rays of the laser beam, performing a collision calculation with each triangle of the geometry mesh [3, p.37]. With the number of triangles k and the beam diameter d_L this leads to a runtime scaling of $\mathcal{O}({d_L}^2 \cdot k)$. This is acceptable for small beams and simple objects like a plate. But for complex geometries and large beams like the ones used for debris removal, this behaviour is quite unsatisfactory. To improve the performance, several approaches have been made:

Coarse collision control

Debris removal is affiliated to uncertainties. This leads to the fact that the laser is not always hitting the object. To prevent unnecessary calculations, a coarse collision control was introduced at the beginning of each shot. Through an orthogonal projection of the debris centre of mass on the line defined by laser position and direction, one can get the distance a between the debris centre and the centre of the laser beam. With the diameter of the laser d_L and of the object d_D, the condition for a hit is

$$a < \frac{d_L}{2} + \frac{d_D}{2} \quad . \tag{3.4}$$

If this is not fulfilled, the beam is not able to reach the target and the calculation can already be stopped at this point, setting $\Delta\vec{p} = 0$ and $\Delta\vec{L} = 0$. However, for Gaussian profiles the fluence outside the diameter d_L is non zero. This may be negligible for small laser energies because the fluence falls under the ablation limit Φ_0, but for laser systems which are assumed for debris removal the fluence in this region is still high enough to induce thrust. Taking this into account, the hit criteria is changed in such a way that the laser diameter d_L is replaced by the radius r_0 at which the fluence is falling below the ablation limit of the material $\Phi_0 = \Phi(r_0)$. Using Equation (1.18) and the definition of the fluence maximum (Equation (1.19)) this leads to the modified criteria

$$a < \sqrt{-\frac{1}{2}\ln\left(\frac{\Phi_0}{\Phi_{max}}\right)} \cdot \frac{d_L}{2} + \frac{d_D}{2} \quad . \tag{3.5}$$

Of course, this leads only to useful results if $\Phi_{max} \geq \Phi_0$. Otherwise the laser is not able to induce momentum at all.

Restrict beamsize to objectsize

Especially for the debris removal scenario, the diameter of the laser beam is usually much larger than the size of the particle $d_D < d_L$. Because the number of rays is quadratic in beam diameter $N = (\frac{d_L}{h_L})^2$, we are tracing many rays which are not able to hit the target. To avoid this, we restrict the beam to the size of the target object. To do so, the centre of mass is projected on the plane defined by the laser position and the laser direction as normal vector. One can get the new beam by cutting out a rectangular piece of the laser profile with edge length d_D. This new beam contains all rays which potentially can hit the target. With the distance to the original laser beam, one can calculate the fluence of each ray. With this improvement, the runtime scales now with d_D^2 instead of d_L^2. For example, if a beam resolution of $h_L = 0.0001m$ and a beam size of $d_L = 1m$ is assumed, we get a total number of rays $N = (\frac{1m}{0.0001m})^2 = 10^8$. With the restriction to the debris size $d_D = 0.1m$, this reduces to $N = 10^6$ and so to a runtime which is two magnitudes faster.

Perform Raytracing on graphics processing unit (GPU)

Even if the number of rays has been decreased, there are still too many rays for a serial CPU calculation. Furthermore, there is a linear scaling in the number of triangles in the geometry mesh k which leads to a problem with complex geometries. Because the calculation of $\Delta\vec{p}_i$ and $\Delta\vec{L}_i$ for each ray i is independent from the other rays, the first problem can be easily handled by parallelization. Therefore, it is a good idea to use the enormous parallelization capabilities of GPUs to perform the raytracing. The second issue can be handled by saving the geometry into a special tree structure in such a way that the rays can be tested in a hierarchical way, instead of testing them always with all k triangles. This division reduces the dependency to $\mathcal{O}(log(k))$ [28, p.183 ff.]. There are several different approaches to create such a tree structure, further discussed for example in [29]. More efficient acceleration structures are often linked to a more performance consuming algorithm, so one has to find the right balance between raytracing performance and structure building performance. However, in this thesis both features are provided by Nvidia Optix [30], a raytracing engine which is able to perform raytracing on GPUs including acceleration structures for geometries.

After performing the above-mentioned collision control and beam-size restriction, followed by creating the rays on device memory, one can perform a "closest hit" tracing with Optix. This tracing will calculate a hit structure for each single ray i which contains

- position of the intersection $\vec{x}_i$
- index of the intersected triangle k_i

The actual physics adopted from Section 1.3.2 is then performed in a self-written CUDA Kernel, calculating $\Delta\vec{p}_i$ and $\Delta\vec{L}_i$ for each ray i in a parallel way. Because the program is using CMS coordinates, the position of the hit can directly be used for the calculation of the angular momentum $\Delta\vec{L}_i = \vec{x}_i \times \Delta\vec{p}_i$. The pre calculated normal vector $\vec{n}_i$ of the surface element can be accessed via the triangle index k_i. Note, that here is actually a performance problem, because all threads are accessing the global device memory containing the triangle data at once, leading to a serialisation of the execution. Nevertheless, runtime studies with the Nvidia performance profiling tool Nsight [31] have shown that the performance of this Section of the code is neglectable comparing to the complete runtime. If a better performance is needed, a better memory management is called for, e.g., using shared memory. Actually, the runtime is already improved by writing the resulting $\Delta\vec{p}_i$ and $\Delta\vec{L}_i$ into one struct, instead of two separate structs thus clustering the memory access. Finally, $\Delta\vec{p}_i$ and $\Delta\vec{L}_i$ are summed up, using the reduce function of the CUDA thrust library [32]. In that way, only 6 floats are copied back to host memory ($\Delta\vec{p}$ and $\Delta\vec{L}$), avoiding so problems with memory bandwidth. Note, that these vectors are still given in CMS system coordinates and have to be rotated back to the ECI system.

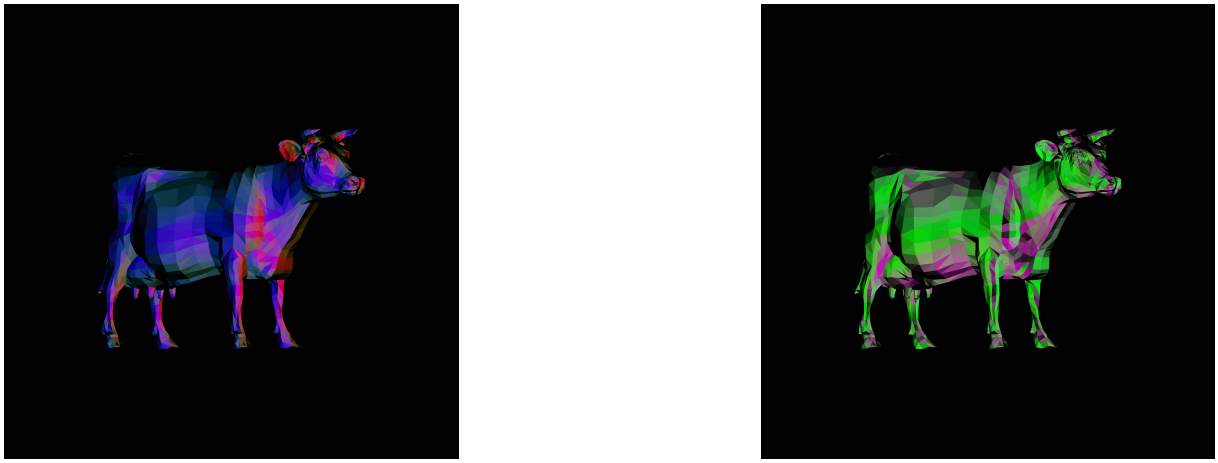

Figure 11: Example for a result of a laser with a constant fluence distribution on a model of a cow. (kindly provided by Nvidia) The brightness corresponds to the amplitude of the (angular)momentum contribution of the corresponding surface element. The colour decodes the direction in CMS. (rgb ↔ xyz). Left: momentum, right: angular momentum

3.4 Python API

Although it is also possible, to control the simulation by changing the parameters in the main function. Permanently recompiling is time consuming and reduces the usability by additional software. The original version of Expedit uses several configuration xml files to handle the problem of continuously recompiling, but still does not provide a sufficient interface for user and software. Because of this, SWIG [33] is used to create an application programming interface (API) for Expedit which offers an easy and comfortable way to perform laser matter interaction calculations by writing python scripts. In Section 2, this API is used to utilize Expedit as a LMI module for orbit propagation simulations. In this section, a short introduction to the API is given: Expedit can be accessed by python code through importing the $'expedit'$ module. To be able to do this, the path of 'expedit.py' and '_expedit.pyd'/'_expedit.so' (Windows/Linux) has to be known by the python interpreter.

```
import expedit
exp = expedit.Expedit()
```

After initialisation, a geometry can be handed over to the software by

```
exp.SetGeometry('plate.obj')
```

The path is relative to the execution path of the script. The geometry is expected to be handed over as Wavefront Object (.obj). This for example can be created with a 3D designing tool like Blender [34]. With one of the following functions, one can set the type of the laser. Note, that all inputs are expected to be in SI units.

```
exp.SetTopHatLaser(diameter, resolution, energy)
exp.SetGaussianLaser(diameter, resolution, energy)
exp.SetFluenceMapLaser(diameter, fluenceMap)
```

For the Gaussian laser, the 'Power in the bucket' definition introduced in Equation (1.16) is used. The fluence map can be handed over as a quatratic $N \times N$ numpy matrix, which contains the fluence for each ray as entry. With the diameter d_L and the matrix dimension N this

defines the resolution $h_L = \frac{d_L}{N}$ and so the energy according to Equation (3.1). The laser-matter interaction parameters for the coupling coefficient introduced in Section 1.2 can be set by

```
exp.SetLMI(a, b, c, phi0, amu, tau, lambda)
```

Then position and orientation of the debris

```
exp.SetDebrisPosition(x,y,z)
exp.SetDebrisOrientation(psi,theta,phi)
```

and position and pointing direction of the laser

```
exp.SetLaserPosition(x,y,z)
exp.SetLaserDirection(x,y,z)
```

should be set. Positions and direction have to be given in ECI or the respective laboratory system. The calculation can then finally initiated by

```
exp.Shoot()
```

This function will eventually throw an error, if not all parameters are set up like mentioned previously. If no error is thrown, the results can be accessed via

```
exp.GetDeltaMomentumX()
exp.GetDeltaMomentumY()
exp.GetDeltaMomentumZ()
exp.GetDeltaAngularMomentumX()
exp.GetDeltaAngularMomentumY()
exp.GetDeltaAngularMomentumZ()
```

Further on, it is possible to plot the results like the ones in Figure 11. To do so, the following function can be used:

```
exp.PrintResult()
```

Note, that not all parameters have to be reset after each calculation. In fact, reloading the geometry will result in a time consuming hard disk access and so to a critical slowdown of the program.

4 Implementation of the Monte Carlo Simulation

Now, that we have got a working implementation of the laser matter interaction, an implementation of the remaining model including the Monte Carlo approach is needed. It is not meant to be a full manual to the code, but to give a rough overview of the simulation input and output format as well as the architecture.

Input/Output

To provide the simulation with the material and geometry, xml files are used containing the debris parameter introduced in Section 2.4.1. The simulation automatically searches for these files in the material and geometry folder within the main simulation directory. The geometry folder includes the triangle data decoded as wavefront-object (.obj), which should have the same file name as the xml file. The orbits of the particles are given by a list with orbital parameter in the TLE format (Section 1.1). Although artificial orbits can be generated by the simulation too. During each simulation, and thus transit, the following quantities are recorded

time	t_i
position	$\vec{x}_i$
velocity	$\vec{v}_i$
angular velocity	$\vec{\omega}_i$
delta momentum	$\Delta\vec{p}_i$
delta angular momentum	$\Delta\vec{L}_i$

which results in a table like the following:

t_1	t_2	...	t_{N-1}	t_N
$\vec{x}_1$	$\vec{x}_2$	...	$\vec{x}_{N-1}$	$\vec{x}_N$
$\vec{v}_1$	$\vec{v}_2$	...	$\vec{v}_{N-1}$	$\vec{v}_N$
$\vec{\omega}_1$	$\vec{\omega}_2$	...	$\vec{\omega}_{N-1}$	$\vec{\omega}_N$
$\Delta\vec{p}_1$	$\Delta\vec{p}_2$	...	$\Delta\vec{p}_{N-1}$	$\Delta\vec{p}_N$
$\Delta\vec{L}_1$	$\Delta\vec{L}_2$	...	$\Delta\vec{L}_{N-1}$	$\Delta\vec{L}_N$

If we include the Monte Carlo part, which is introduced in Section 2.5 this leads to a cube with three dimensions: first the property (time, position, velocity etc.), the number of the pulse (respective the indices i) and the number of the Monte Carlo run. For saving this data cube, the Fits Format is chosen [35]. The Fits format is an image format heavily used in astronomy and allows to save several images, tables or datacubes with headers in an ordered and easily accessible way. This means, that the results of several Monte Carlo simulations can be stored within one file. The data can then be analyzed afterwards by using the astropy.fits package. With this design, the simulation and the analysis of the results are completely separated.

Simulation Architecture

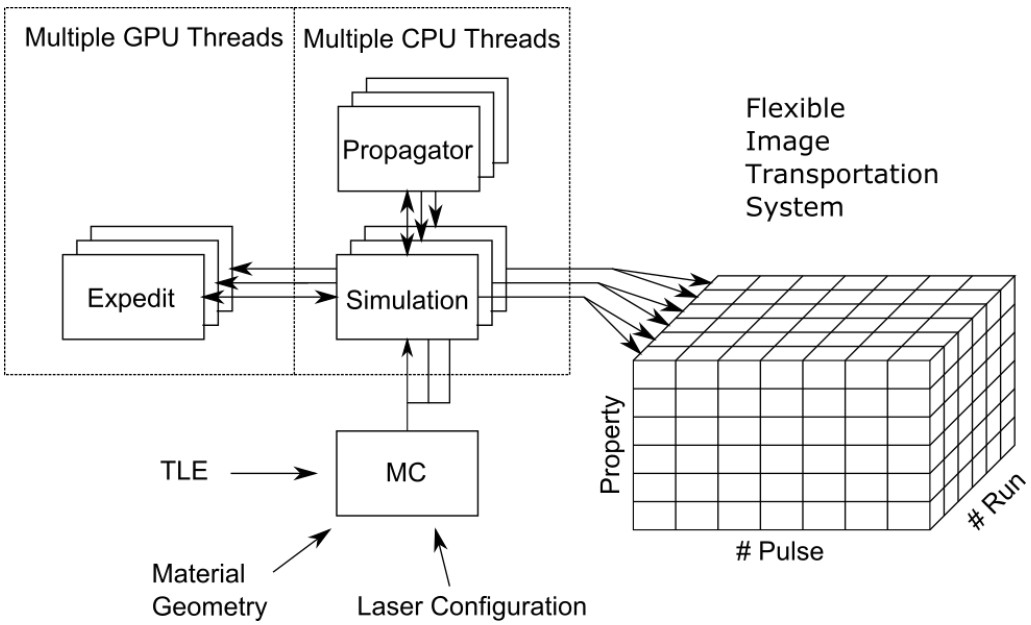

Figure 12: Schematic design of the complete simulation including the LMI module 'Expedit' and the C++ propagators. Note, that the Monte Carlo (MC) steps are independent from each other so one can use multiple CPU threads. Each CPU instance of Expedit creates many GPU threads. (one for each ray)

The core simulation is written in python in an object-oriented way. This allows easy reusability in later applications. For example, it is easy to implement a space-based laser station instead. Because of performance reasons, both propagators are written in C++ by using again Swig as a wrapper to python.

As already mentioned in Section 2.2.1, the astropy package is used to calculate the sidereal angle γ at each step. Runtime tests show, that this way is rather slow. Because of this, the angle is only calculated at the start of the simulation in an explicit way. During the simulation it is propagated stepwise by using $\gamma_{i+1} = \gamma_i + \omega_E h$ with the average rotation speed ω_E of the earth and h as the model step size. Regarding the rotation propagator, it was found that the algorithm performs more stable if the units are scaled to the CGS system (Centimeter Gramm Seconds) in before.

Because all Monte Carlo runs are independent from each other, a second layer of parallelization is introduced by using multiple CPU threads. Each thread has its own instance of the simulation, enclosing expedit and both propagators. The boundary conditions are the same for all threads, but they differ in the random variables. Each thread results in a transit and so to a column of the final data cube. To reduce the overhead created by thread creation and convergence testing, every thread performs several transits until the results are tested on convergence.

5 Code Validation

Before starting with further simulations, it seems advisable to perform some validation runs to compare the results to analytical and experimental data. Furthermore, appropriate values for the propagator step sizes h_{orb}, h_{rot} and beam resolution h_L must be determined.

5.1 Mesh convergence study

First of all, we want to examine a suiting value for the beam resolution parameter used by Expedit in Section 3. To gain a value which performs well for arbitrary objects, a rather complex geometry is chosen which contains fine structures and round surface elements: A paper bin shown in Figure 13. To get values which are also valid for the conditions within the simulations

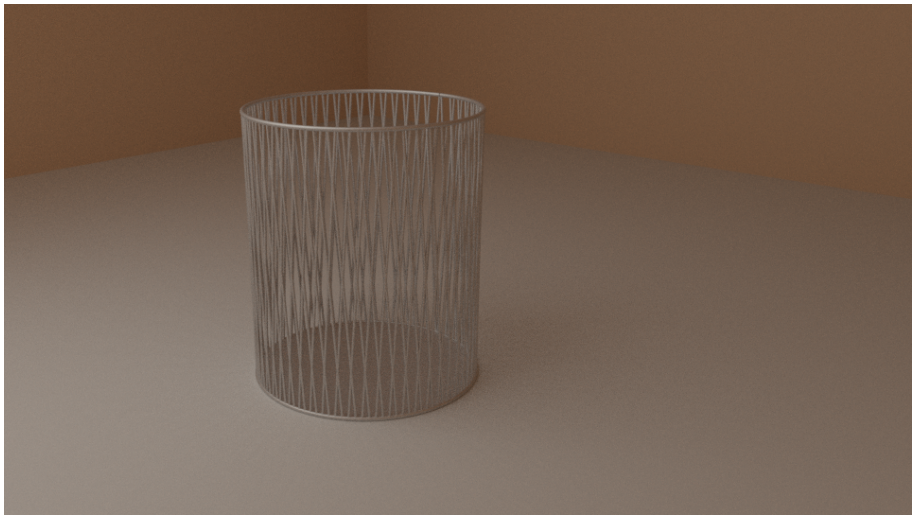

Figure 13: Paper bin, designed by Stefanie Meiritz. The rendering was made with Blender.

in Section 6, similar parameters are used: A laser energy of $E_L = 50kJ$ and a Gaussian profile with a diameter of $d_L = 1m$ are assumed. To get a similar target size the bin is narrowed down to $15cm$. Several runs were made with resolutions $h_L \in [0.01, 0.0001]$ plotting $|\Delta\vec{p}|$, $|\Delta\vec{L}|$ Figure

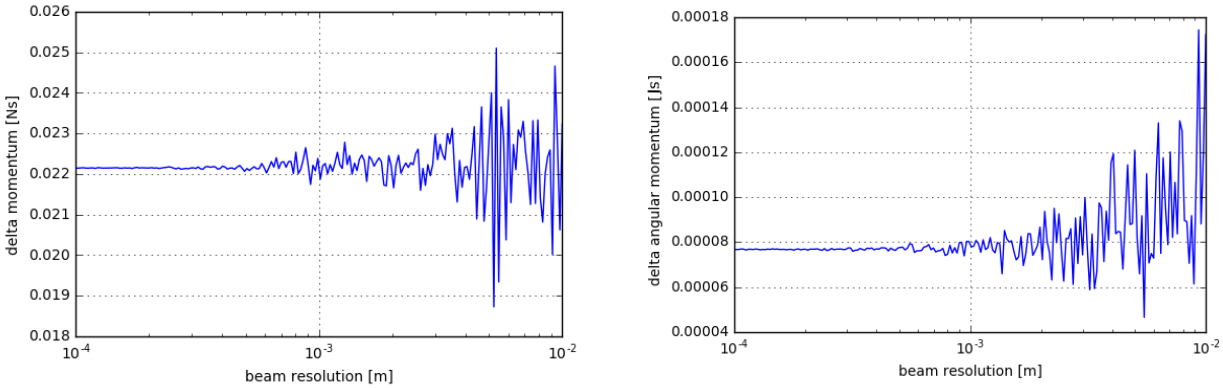

Figure 14: Left: Induced momentum change $\Delta|\vec{p}|$. Right: Induced change in angular momentum $\Delta|\vec{L}|$. Plotted over the beam resolution h_L.

14 shows, that the results converge for $h_L < 0.001m$. For the following simulations, a resolution

of $h_L = 0.0001m$ is chosen. This behaviour was also observed for simpler objects like plates although the effects of large beam resolution is much more dependent on the orientation: If edges are aligned perpendicular to the ray rows, a complete row of rays can slip of or slip on the target by changing the resolution which causes a sudden change in momentum. Furthermore, the runtime is recorded for each beam resolution and plotted in Figure 15. For $h_L > 0.001m$

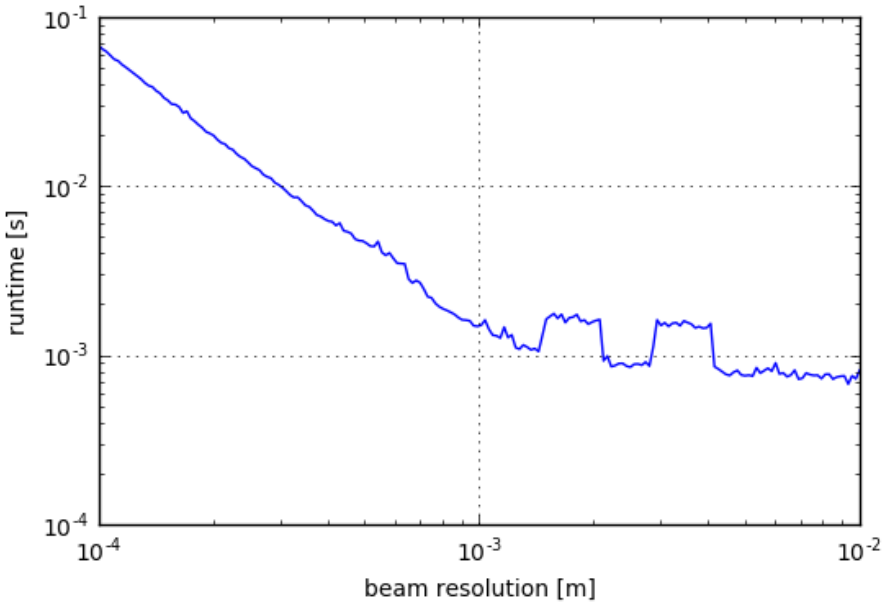

Figure 15: Logarithmic plot of runtime over beam resolution. The Code was run with a NVIDIA GeForce GTX 570.

one can see, that the program overhead is dominating. For $h_L < 0.001m$ the expected runtime scaling, proportional to the number of rays $N \propto \frac{1}{{h_L}^2}$, can be observed. The peaks in runtime are probable artefacts within the CUDA API caused by interferences with the memory access. But these performance dips have no relevant influence and do not need to be investigated further.

5.2 Experimental validation of Expedit

The whole theory introduced in Section 1.2 and the simulation Expedit was tested in cooperation with the GSI Helmholtz Centre for Heavy Ion Research in Darmstadt. [36] To do so, the

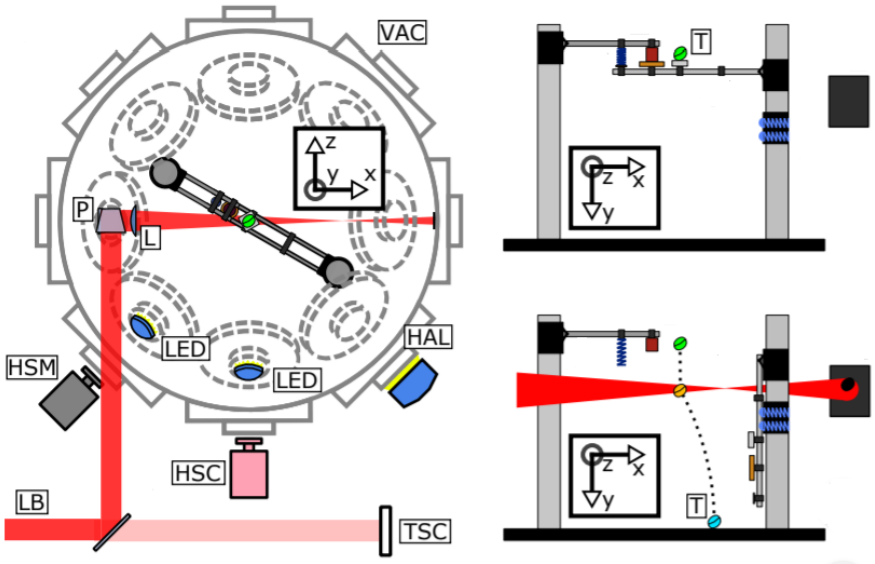

Figure 16: Experimental setup, taken from Figure 1 in [36]. Left top view, right view from the side. The laser beam (LB) is directed at a target object (T) which falls in a vacuum chamber (VAC)

Nanosecond High Energy Laser for Heavy Ion Experiments ('nhelix') was used to irradiate free-falling targets (T) in a vacuum chamber. The movement of the target was recorded by two high speed cameras (HSM/HSC) allowing to track the velocity $\vec{v}(t)$ and angular velocity $\vec{\omega}(t)$ of the target over time t. Placed on a free fall arm, the start conditions of the target were $\vec{v}(0) = 0$ and $\vec{\omega}(0) = 0$. Because the target is falling in a vacuum chamber the dynamics without the Laser shot can be easily described by

$$\vec{v}(t) = g\,t \cdot \vec{e}_y \tag{5.1}$$

$$\vec{\omega}(t) = 0 \quad . \tag{5.2}$$

Applying now one laser shot exactly (or to be really exact, as exact as possible) when the target is centred in the laser beam leads to an additional change in velocity $\Delta\vec{v}$ and an angular velocity $\Delta\vec{\omega}$ which can be measured. For this experiment, a pulse energy of $80J$ a pulse length τ of $10ns$ and a spot beam size of approx. $3cm$ was chosen to ensure that the fluence at the target is close to the fluence we expect to have in later debris removal scenarios. Overall, 6 different target configurations are used for the code validation:

Target	Material	Orientation
L Profile	Aluminium	bend to laser
L Profile	Aluminium	bend from laser
Cylinder	Aluminium	centred
Plate	Aluminium	0° angle of incidence
Plate	Aluminium	30° angle of incidence

Because the laser system is only able to perform one shot per hour, only a few repetitions per target configuration was possible. For the comparison with the simulation, the same configurations are modeled by using information about the beam profile (refer to Section 3.2) and the orientation/position of the target in the beam. This is possible by analysing the negative picture produced by the shot. In Figure 17 one can see, that there is a general agreement between

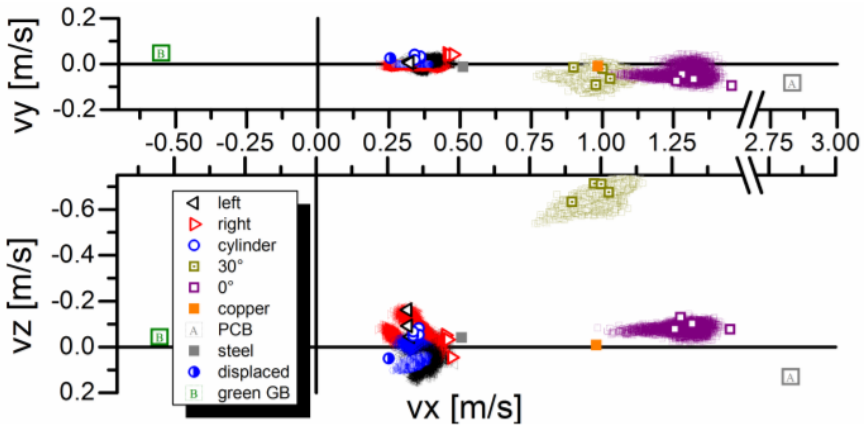

Figure 17: Experimental results compared to simulation results, adapted from Figure 4 in [36]. Symbols denote the resulting velocity measured in the experiment. To take care of uncertainties in start conditions the simulations are repeated several times with slightly different initial conditions leading to same coloured point clouds for each object.

experiment and simulation. The main deviations can be seen in the difference in Δv_z between the bend to laser and bend from laser L profile which can be explained by an additional nozzle effect which is not accurately described by Expedit. Furthermore, one of the 0° plates quite offset to the other three plates. This can be explained by a faulty tracking of the target object. Regarding the rotational velocities, the simulation shows that the actual uncertainty is too large to be compared to the measured values. If the uncertainty of pointing and initial orientation are taken into account, the cloud becomes too large to derive meaningful insights. To improve this, further experiments are planned to increase precision in measurement.

5.3 Propagator validation

To verify that the propagator is working correctly, an object placed $600km$ above the earth surface is propagated on a circular orbit for four hours by using the first cosmical velocity v_circ tangential to the earth surface. This velocity can be calculated by equalizing the gravitational force in Equation (2.41) and the centripetal force $F_{cent} = F_{grav}$ which leads to

$$v_{circ} = \sqrt{\frac{\mu}{|\vec{x}|}} \quad . \tag{5.3}$$

During the simulation, altitude and energy (Equation (1.1)) are measured. Because both values should stay constant for an undisturbed circular orbit, the error can be easily gained by subtraction from the initial values. According to Figure 18, a step size $h_{orb} = 0.1s$ is sufficient,

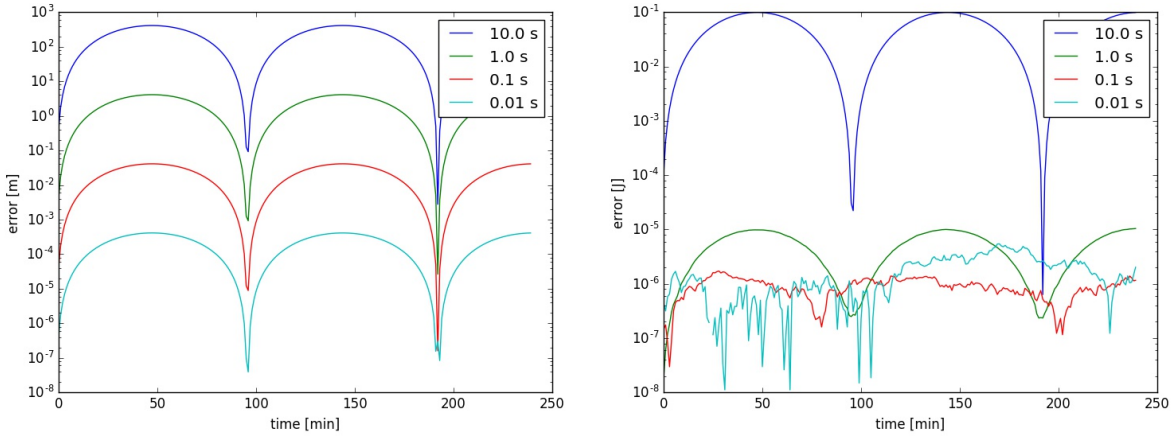

Figure 18: Left: absolute error in height. Right: absolute error in energy. Several step sizes h_{orb} are plotted in different colours.

because only short transits under 10 minutes are considered in this thesis.

Further on, we want to validate the rotation propagator and investigate how long one can propagate the orientation until the error reaches a critical level. The rotation of a plate, the same which was used in the experiment in Section 5.2, is propagated for 10 minutes, plotting the error in rotational energy over time. The energy of a rotating object is

$$E_{rot} = \frac{1}{2}\vec{L}\cdot\vec{\omega} \tag{5.4}$$

with the angular momentum $\vec{L}$ and the rotational velocity vector ω. Because the energy should be conserved during the undisturbed rotation, one can get the relative error of the propagation

$$\epsilon = \frac{|E_{rot} - E_{init}|}{|E_{init}|}. \tag{5.5}$$

For $h_{rot} = 0.01$ and $h_{rot} = 0.005$ and averaged over 1000 random initial orientations the results are shown in Figure 19. The plot shows that it is sufficient to use $h_{rot} = 0.01$ as step size for small velocities. With this one can simulate rotations of up to $20\frac{rad}{s}$. If we want to simulate higher rotational velocities $h_{rot} = 0.005$ is needed.

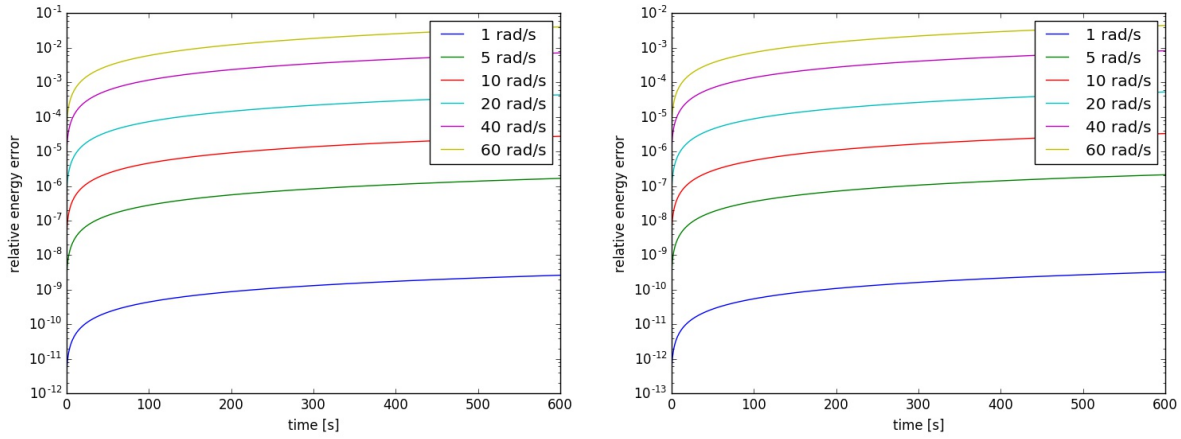

Figure 19: Energy error over time for several initial rotation speeds decoded by colours. Left: $h_{rot} = 0.01$ Right: $h_{rot} = 0.005$

5.4 Validation of Orbit modification calculations

For the validation of the whole simulation process (including orbit propagation, momentum calculation and perigee/apogee calculation) one can use following formula derived by [37, p. 895-915]

$$\frac{dv}{dt} = \frac{c_m I s^2}{m_D} \quad . \tag{5.6}$$

This analytical formula gives the acceleration for a cube with the edge length s and mass m_D under laser radiation with intensity I, assuming a constant coupling coefficient c_m. Note, this equation is invariant under rotations. Again, we are interested in the change in velocity for a single pulse with pulse length τ. Integration is leading to

$$\Delta v = \int_0^\tau \frac{dv(t)}{dt} dt = \int_0^\tau \frac{c_m I(t) s^2}{m_D} dt = \frac{c_m \Phi s^2}{m_D} \tag{5.7}$$

with the laser fluence Φ. Now we have to find a constellation which can be applied to the analytical formula and the numerical simulation as well. For the target object we use the parameter for a typical CubeSat [38] and laser parameter which are matching to a $50kJ$ laser with $20cm$ diameter and a constant fluence profile. Summarized, the parameters are:

s	$10cm$
m_D	$0.2712kg$
Φ	$0.159kJ/cm^2$
c_m	$25\frac{\mu Ns}{J}$

To make the analytical solution easier, we assume a circular orbit with a height of $600km$ and send N laser pulses directly from below (this means, the cube is at the zenith). The velocity of the cube after N pulses is then in ECI

$$\vec{v} = \begin{pmatrix} 0 \\ v_{circ} \\ N \cdot \Delta v \end{pmatrix} \quad . \tag{5.8}$$

Together with the position

$$\vec{x} = \begin{pmatrix} 0 \\ 0 \\ 600 \end{pmatrix} km \tag{5.9}$$

one can use the formula introduced in Section 1.1 to calculate perigee x_p and apogee x_a. The same configuration can now be numerically implemented. To test the whole functionality of the simulation, it seems advisable not to create an artificial situation just for the validation. So we shoot on the moving cube in a small interval around the zenith $[\pi - \frac{\epsilon}{2}, \pi + \frac{\epsilon}{2}]$. One would expect the results to converge to the analytical solution for $\epsilon \to 0$. We keep the repetition rate constant at $10Hz$, so the number of pulses arriving at the target are varying according to ϵ. Fig-

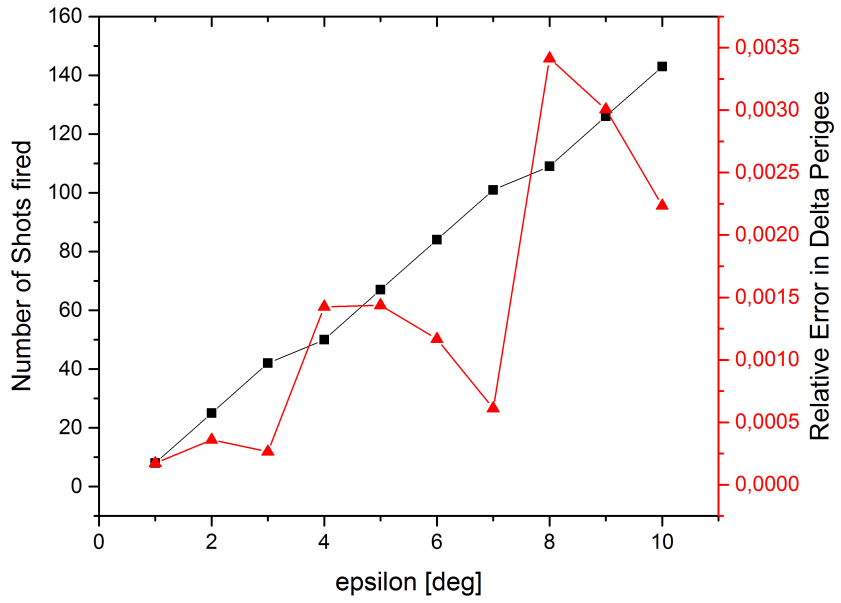

Figure 20: Relative error in Δx_p between simulation and analytical solution(red) and the number of pulses send(black). It is plotted over different values for ϵ.

ure 20 implies, that the results follow the predicted analytical values. The relative error shows a linear behaviour to the increasing number in pulses. The deviations arise from a ϵ depending offset to the initial cube position which was investigated and solved later on. Even if this is an artificial and simplified test, it implies that the implementation is basically correct.

6 Monte Carlo Studies on laser-induced orbit modification

6.1 Introduction

Finally, the developed tools are now used to investigate the behaviour of space debris under laser irradiation. To keep the study simple we will restrict the investigation to one laser configuration which is based on the CleanSpace study [22]

spot diameter d_L	$1m$
pulse energy E_L	$50kJ$
wavelength λ	$1064nm$
pulse length τ	$10ns$
repetition rate f	$10Hz$

According to Section 1.1, aluminium is the most common material and so a natural choice for the studies. An abstract parametrization of the shape was introduced in Section 1.1. The object is set on a circular LEO orbit ($700km$ height) which moves directly through the zenith above the laser station. We perform Monte Carlo simulations with a maximum of 10000 samples. The simulation should stop when the relative error $\frac{\epsilon_0}{x_p}$ in perigee x_p is smaller than 10^{-4}. Each single Monte Carlo simulation leads to results like illustrated in Figure 21. Although the height

d

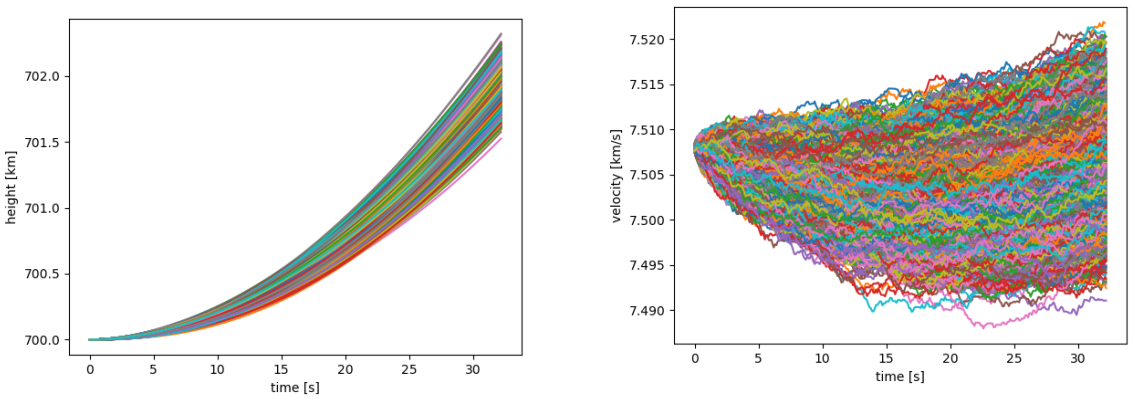

Figure 21: Final result of a plate, illuminated from 80° to 100°. Each line stands for a single transit within a Monte Carlo simulation. Left: Particle height over transit time. Right: Particle velocity over transit time.

of the object always increases during the transit, the velocity is mostly decreasing and so is the perigee x_p. In the following, we use the values after the last time step to calculate the final perigee. Mean and standard values of the perigee are calculated and then compared between the different initial conditions.

6.2 Influence of initial rotation and laser pointing accuracy

First, we want to estimate the influence of the initial rotation and laser accuracy. To ensure comparability, all targets are put on the same simple circular orbit with a direct transit over the laser station. To fulfill the assumptions from Equation (2.14), we keep the zenith angle ζ small and start the simulation with an elevation of 80° and stop at 100°. As values for the initial rotation frequency the full range from $0Hz$ up to $10Hz$ is chosen. Additionally, we simulate a run without rotation at all by picking a random orientation at each step i. The laser accuracy ranges

from values which imply a hundred percent chance of hit (we refer to Figure 9). The maximum σ and so the maximal uncertainty is selected according to a worst case scenario gained with the values from Equation (2.17). As geometries, we use some of the simple geometries from the experiments in Darmstadt (Section 5.2): A plate, a wedge and a sphere ($2cm$ diameter each) as well.

The results of the study are presented in Figure 22. For each geometry a plot is created where the x axis denotes the laser accuracy and the y axis the final change in perigee. The different rotational frequencies are printed in different colours, the random run is marked with dash lines. In total, one can see that the distinction between different initial rotational speeds is more important for high pointing accuracies. The resulting change in perigee is smallest for the sphere. This is due to the low $\frac{A}{m}$ ratio of the sphere. On the other side, the error is near 0 and the results are as expected independent from the rotation (neglecting errors from the discretisation). For the plate in contrast, a quite strong dependency is visible. The mean varies over $60km$ and the error is quite large. Nevertheless it can be seen, that the expected perigee is almost always lowered. The results gained with random orientations lead to a quite nice approximation of the mean, but completely fail for the error prediction. The results for the wedge are quite similar to the one of the plate but smaller due to the lower area mass ratio. The dependency on the rotational speed is unexpectedly small and could be completely neglected. Just the error for rotation frequencies up to $10Hz$ lead to a significant different result. There have to be further simulations to test, if this is a physically correct behaviour or due to numerical errors.

6.3 Influence of the shape

As next step, we want to estimate the influence of different debris shapes. To replicate appropriate geometries, a program was developed to generate ellipsoids with the three axis fulfilling the observed restrictions. In total, 100 plates and rods are generated. The agreement with the experiments are represented in Figure 23 by red dots. To keep the simulation runtime practicable, the initial rotational speed and the accuracy are fixed for all targets. As speed $1Hz$ is chosen and the laser pointing accuracy is set to $4\mu rad$ which is the accuracy which was estimated in Section 2.2.2. The results in Figure 24 are plotted over the area mass ratio of the corresponding targets. The two groups of ellipsoids (plates and rods) are still visible: the rods form the top of the graph and the plates form a bulk on the left below. The plate like shapes lead to a significant stronger lowering of the perigee. For both groups the expected trend can be seen, that higher area mass ratios cause lower perigees.

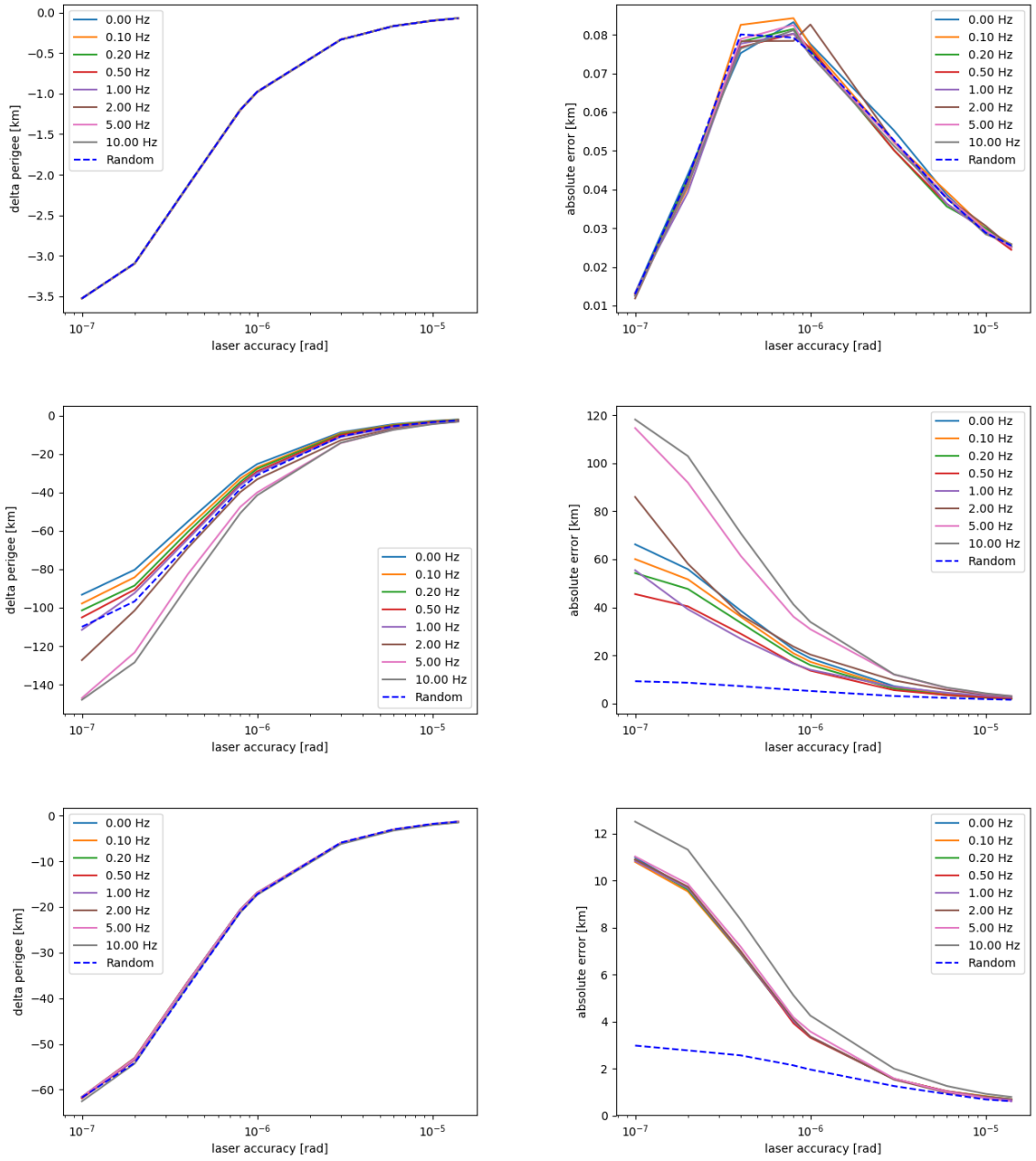

Figure 22: Left column: change in perigee plotted over the laser accuracy for the sphere, the plate and the wedge (from top to bottom). The errors are plotted separately in the right column. The different initial angular speeds are decoded by different colours. The results from runs with random orientations are marked with dash lines.

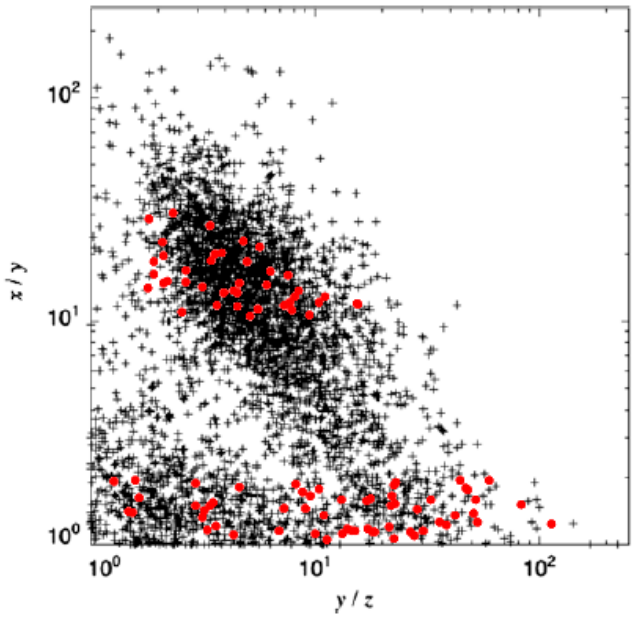

Figure 23: Overlay of Figure 2 with the generated ellipsoid used in the study represented by red dots.

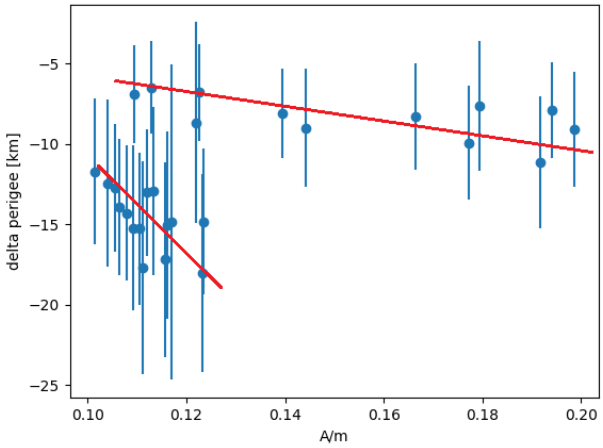

Figure 24: Resulting change in orbit, plotted over the area mass ratio of the corresponding ellipsoids. The error bars represent the standard derivations of the expectation value. Trend lines are introduced to highlight linear behaviour in A/m.

7 Summary and Outlook

In this thesis, the laser-matter interaction tool 'Expedit' is improved and heavily accelerated, leading so to a tool suitable for debris orbit alternation calculations with high repetition laser pulses. To estimate the change of the resulting orbit in a Laser-Based Debris Removal scenario, this tool is used in a Monte Carlo approach. Because the shape is expected to play an important role in the alternation process, the rotation is included into the model as well. Additional attempts are made to pay attention to the influence of the atmosphere on the pointing accuracy. The developed tools are finally used to investigate the behaviour of randomly generated objects in a simplified removal scenario.

The results suggest that the perigee of space debris targets is reliably lowered assuming a direct transit over the laser station. This effect is especially large for plate-like objects with a high area-mass ratio. The rotational speed heavily affects the outcoming results, in particular for high laser pointing accuracies. Regarding the spread of the resulting orbits, future investigations are necessary including a set of real measured space debris orbits. Here it seems also advisable to use CAD models of debris particle which arose from crash test experiments. One important need in refinement is the beam propagation. The estimated Gaussian profile is far from reality and the beam wander effect is just based on a rough estimation. Thus, a full simulation of the propagating beam through the atmosphere is mandatory. A further refinement of the laser matter interaction could be the consideration of reflections in the raytracing algorithm which could cause a stronger recoil than predicted by the actual algorithm [36].

A further aspect, which was not discussed in this thesis, is the heating of the target due to the incoming laser irradiation. Melting the target could lead to the formation of a sphere which has a negative influence on the amount of induced momentum (refer to the simulation results) on the target and the ability for tracking them [39]. Furthermore, the target could be ripped apart, leading so to smaller but still dangerous particles, which are even harder to detect. Although this effect is not part of this thesis, it was introduced to the code by the author, making further numerical investigations on this topic possible, too [13] [40].

References

[1] *SPACE DEBRIS: THE ESA APPROACH*. March 2017. ISBN 978-92-9221-104-2.

[2] Q. Wen, L. Yang, S. Zhao, Y. Fang, and Y. Wang. Impacts of orbital elements of space-based laser station on small scale space debris removal. *Optik 154*, 2017.

[3] J. Wilken. Modelling of laser-based thrust generation for space debris removal. Master thesis, Technische Universität Braunschweig, January 2015.

[4] H. D. Curtis. *Orbital Mechanics for Engineering Students, Third Edition (Aerospace Engineering)*. Butterworth-Heinemann, 2013. ISBN 0080977472.

[5] C. R. Phipps. Removing orbital debris with lasers. *Advances in Space Research 49*, 2012.

[6] Celestrak. `https://www.celestrak.com/`. accessed 18.12.2017.

[7] J.N. Opiela. A study of the material density distribution of space debris. *Advances in Space Research 49*, 2009.

[8] T. Hanada, J.-C. Liou, T. Nakajima, and E. Stansbery. Outcome of recent satellite impact experiments. *Advances in Space Research*, 44(5):558 – 567, 2009. ISSN 0273-1177. doi: 10.1016/j.asr.2009.04.016.

[9] D. J. Kessler, N. L. Johnson, J.-C Liou, and M. Matney. The kessler syndrome: Implications to future space operations. *Advances in the Astronautical Sciences*, 137, Jan 2010.

[10] C. Phipps, M. Birkan, W. Bohn, H.-A. Eckel, H. Horisawa, T. Lippert, M. Michaelis, Yu. Rezunkov, A. Sasoh, W. Schall, S. Scharring, and J. Sinko. Review: Laser-ablation propulsion. *Journal of Propulsion and Power 26*, 2010.

[11] D.A. Liedahl et al. Pulsed laser interactions with space debris: Target shape effects. *Advances in Space Research 52*, 2013.

[12] M. E. Povarnitsyn, N. E. Andreev, P. R. Levashov, K. V. Khishchenko, and O. N. Rosmej. Dynamics of thin metal foils irradiated by moderate-contrast high-intensity laser beams. *Physics of Plasmas 19*, 2012.

[13] S. Scharring, R.-A. Lorbeer L. Eisert, and H.-A. Eckel. Momentum predictability and heat accumulation in laser-based space debris removal. Submitted for High Power Laser Ablation, Santa Fe, NM, 26.-29.3.2018, 2018.

[14] D.A. Liedahl, S. B. Libby, and A. Rubenchik. Momentum transfer by laser ablation of irregularly shaped space debris. *AIP Conference Proceedings 1278, 772*, 2010.

[15] Spg4 propagator. `https://pypi.python.org/pypi/sgp4/`. accessed 27.12.2017.

[16] Larry C. Andrews and R. L. Phillips. *Laser Beam Propagation through Random Media, Second Edition (SPIE Press Monograph Vol. PM152)*. SPIE Publications, 2005. ISBN 0819459488.

[17] Astropy. `http://docs.astropy.org/en/stable/`. accessed 20.12.2017.

[18] S. Scharring, J. Wilken, and H.-A. Eckel. Laser-based removal of irregularly shaped space debris. *Optical Engineering 56*, 2017.

[19] W. Riede, D. Hampf, P. Wagner, and A. Giesen. Laserbasierte ortung von weltraumschrott. http://elib.dlr.de/94160/1/Laserbasierte%20Ortung%20von%20Weltraumschrott_Riede_DLR.pdf. accessed 27.12.2017.

[20] ESO VLT Performance. https://www.eso.org/sci/facilities/paranal/telescopes/ut/utperformance.html. accessed 30.10.2017.

[21] Isaac newton group of telescopes pointing error. http://www.ing.iac.es/Astronomy/telescopes/wht/pointing.html. accessed 16.11.2017.

[22] B. Esmiller, C. Jacquelard, H.-A. Eckel, and E. Wnuk. Space debris removal by ground-based lasers: main conclusions of the european project cleanspace. *Applied Optics*, 53 (31):45–54, Nov 2014. doi: 10.1364/AO.53.000I45.

[23] Josef Honerkamp and Hartmann Römer. *Klassische Theoretische Physik: Eine Einführung (Springer-Lehrbuch) (German Edition)*. Springer Berlin, 2012. ISBN 3642232612.

[24] Stefan Gerlach. *Computerphysik: Einführung, Beispiele und Anwendungen (German Edition)*. Springer Spektrum, 2016. ISBN 978-3-662-49429-5.

[25] S. R. Buss. Accurate and efficient simulation of rigid-body rotations. *Journal of Computational Physics 164*, 2000.

[26] Ilja N. Bronstein, Konstantin A. Semendjajew, Gerhard Musiol, and Heiner Mühlig. *Taschenbuch der Mathematik*. Verlag Harri Deutsch, Frankfurt am Main, 2000. ISBN 3817120052.

[27] Ulrich Krengel. *Einführung in die Wahrscheinlichkeitstheorie und Statistik*. Springer Science + Business Media, 2005. ISBN 978-33-2292-860-3.

[28] Matt Pharr, Wenzel Jakob, and Greg Humphreys. *Physically Based Rendering, Third Edition: From Theory to Implementation*. Morgan Kaufmann, 2016. ISBN 0128006455.

[29] I. Wald and V. Havran. On building fast kd-trees for ray tracing, and on doing that in o(n log n). In *IN PROCEEDINGS OF THE 2006 IEEE SYMPOSIUM ON INTERACTIVE RAY TRACING*, pages 61–70, 2006.

[30] S. G. Parker, J. Bigler, A. Dietrich, H. Friedrich, J. Hoberock, D. Luebke, D. McAllister, M. McGuire, K. Morley, A. Robison, and M. Stich. Optix: A general purpose ray tracing engine. *ACM Transactions on Graphics*, August 2010.

[31] Nvidia nsight. http://www.nvidia.com/object/nsight.html. accessed 18.09.2017.

[32] Nvidia thrust library. https://developer.nvidia.com/thrust. accessed 18.09.2017.

[33] Simplified wrapper and interface generator (swig). http://www.swig.org/. accessed 05.07.2017.

[34] Blender. https://www.blender.org/. accessed 18.09.2017.

[35] Fits file handling. http://docs.astropy.org/en/stable/io/fits/. accessed 20.12.2017.

[36] R.-A. Lorbeer, M. Zwilich, M. Zabic, S. Scharring, L. Eisert, J. Wilken, D. Schumacher, M. Roth, and H.-A. Eckel. Experimental verification of high energy laser-generated impulse for remote laser control of space debris - learn to control the force. Submitted for Scientific Reports.

[37] D.A. Liedahl, A. Rubenchik, S. Nikolaev S.B. Libby, and C.R. Phipps. Pulsed laser interactions with space debris: Target shape effects. *Advances in Space Research 52*, 2013.

[38] Cubesat. `http://www.cubesat.org/`. accessed 07.08.2017.

[39] S. Scharring, R.-A. Lorbeer, and H.-A. Eckel. Heat accumulation in laser-based removal of space debris. *AIAA Journal*, 2018. doi: 10.2514/1.J056718.

[40] R.-A. Lorbeer et al. Laser-based space debris removal - laser-induced momentum generation on true scale debris-like targets. Poster, High Power Laser Ablation, Santa Fe, NM, 26.-29.3.2018.